Lateral Ion Migration Accelerates Degradation in Halide Perovskite Devices

Daniel A. Jacobs[a], Christian M. Wolff[a], Xin-Yu Chin[b], Kerem Artuk[a], Christophe Ballif[a,b], Quentin Jeangros[b]

[a] *Ecole Polytechnique Fédérale de Lausanne (EPFL), Institute of Electrical and Micro Engineering (IEM), Photovoltaics and Thin-Film Electronics Laboratory (PV-Lab),*
Neuchâtel, Switzerland.
[b] *CSEM, Sustainable Energy Center, Neuchâtel, Switzerland*

Supporting Information

Contents:

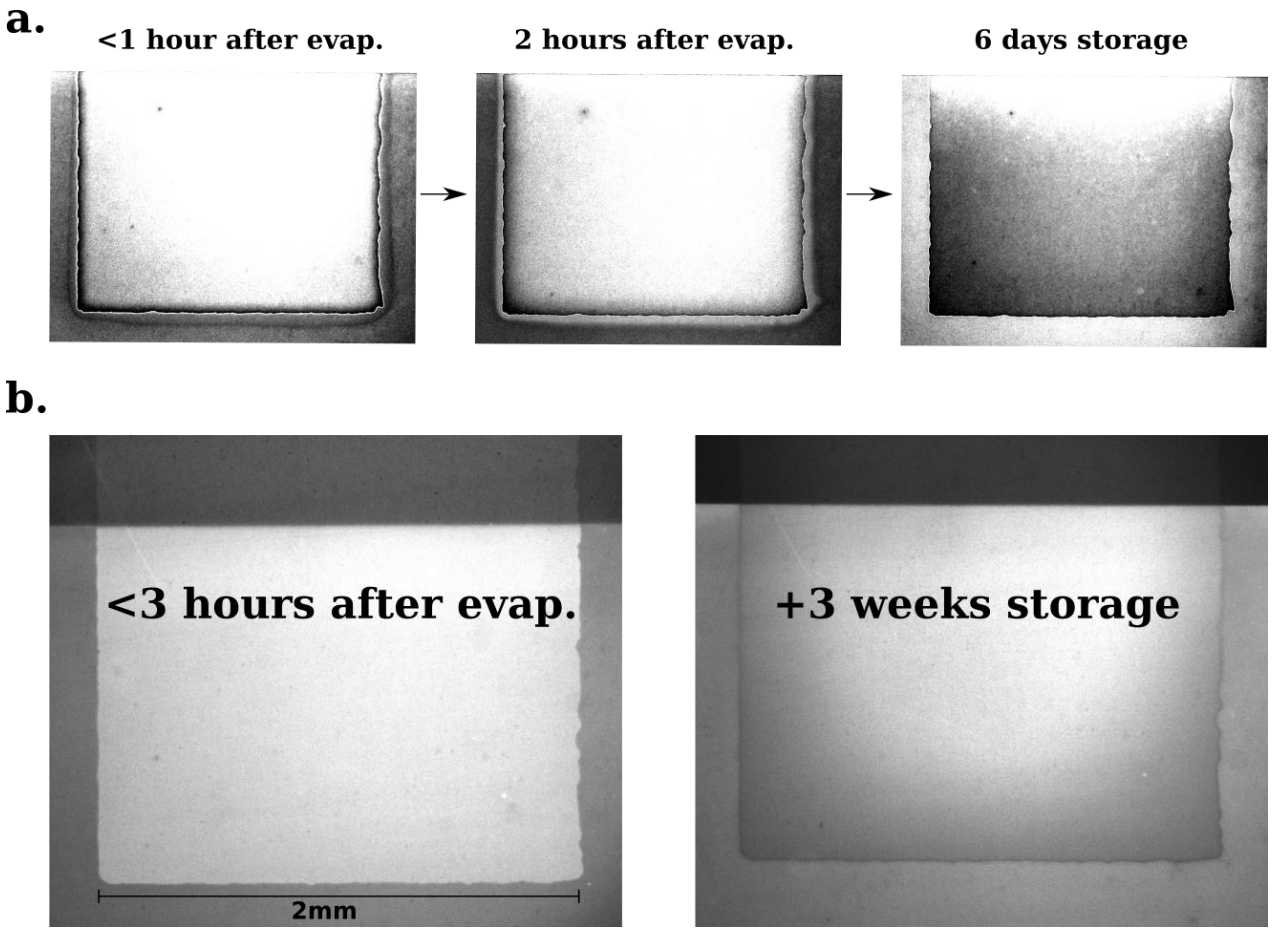

Supplementary Figure 1. Edge effects in the resting state. (a) PL images of a solar cell device at various times after evaporating the top (Ag) electrode. Contrast and brightness have been scaled independently inside and outside the active area in these images to display edge effects in both regions. A dark front can be seen intruding on the active area as early as 1 hour after deposition of the top electrode (left). Following the first image, the device was placed in a nitrogen glovebox for ~1hour, after which the second image was taken. The device was then placed back in storage and imaged again 6 days layer (third image). (b) Un-adjusted PL images showing the same device shortly after evaporation of the top electrode and after 3 weeks in inert-gas storage.

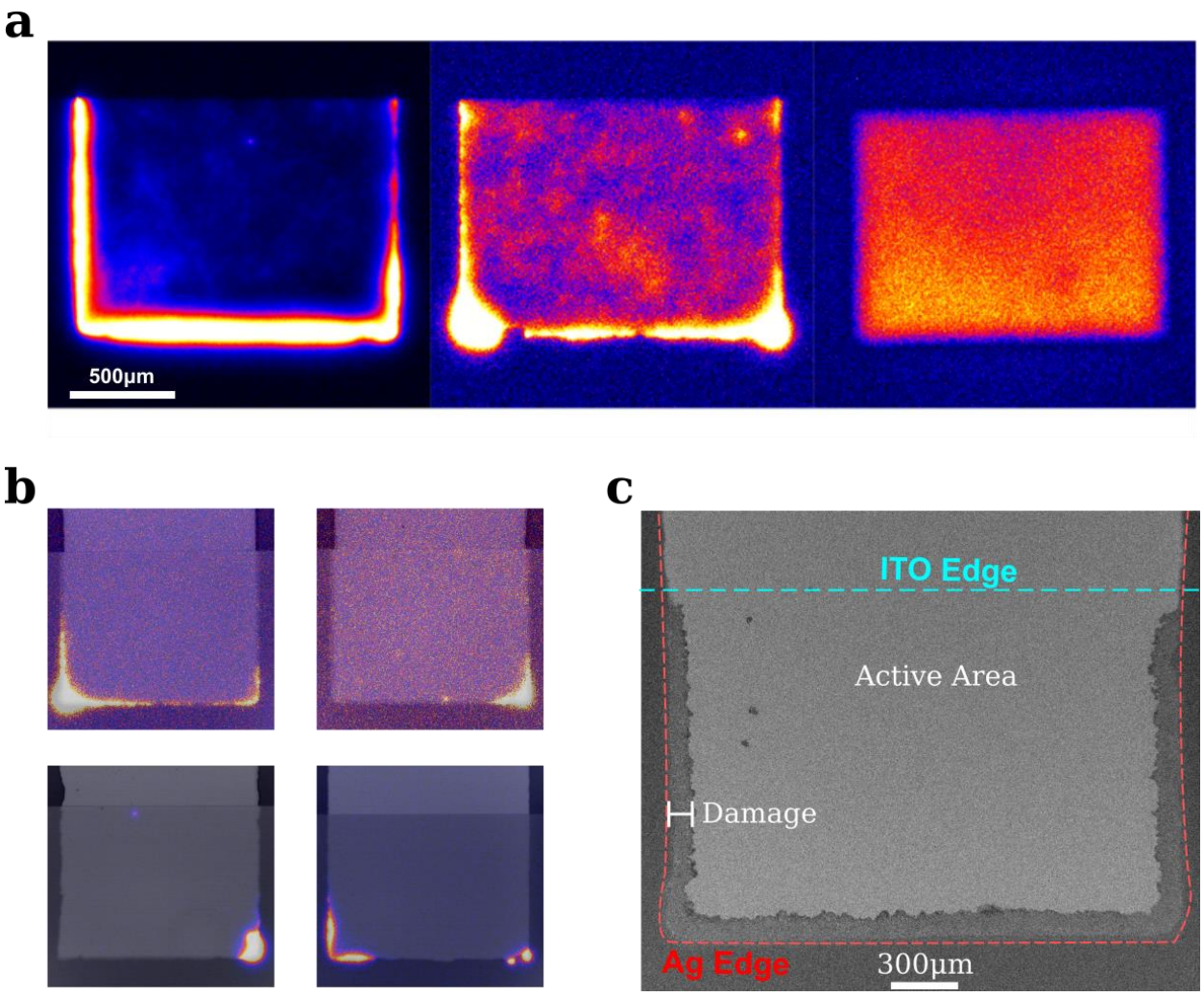

Supplementary Figure 2. Preliminary observations of edge breakdown and degradation during reverse-bias testing. (a) Lock-in thermography images (-4V, 25Hz) of three pixels on the same substrate, showing qualitatively different patterns of reverse-breakdown. The origin of this intense variability is presently unknown, but might be related to substrate gradients induced during thermal evaporation of the $CsBrPbI_2$ template, or during the metal electrode deposition (small changes in mask height above the substrate change the sharpness of electrode boundaries, which may in turn influence the strength of lateral electric fields). (b) More examples of edge and corner-specific breakdown (c.f. Supp. Fig. 3 where we show that mobile anions accumulate preferentially at corners/sharp features of the electrode). (c) SEM micrograph showing severe damage surrounding the n-boundary (Ag edge) of a solar cell following a reverse-bias test at -4V.

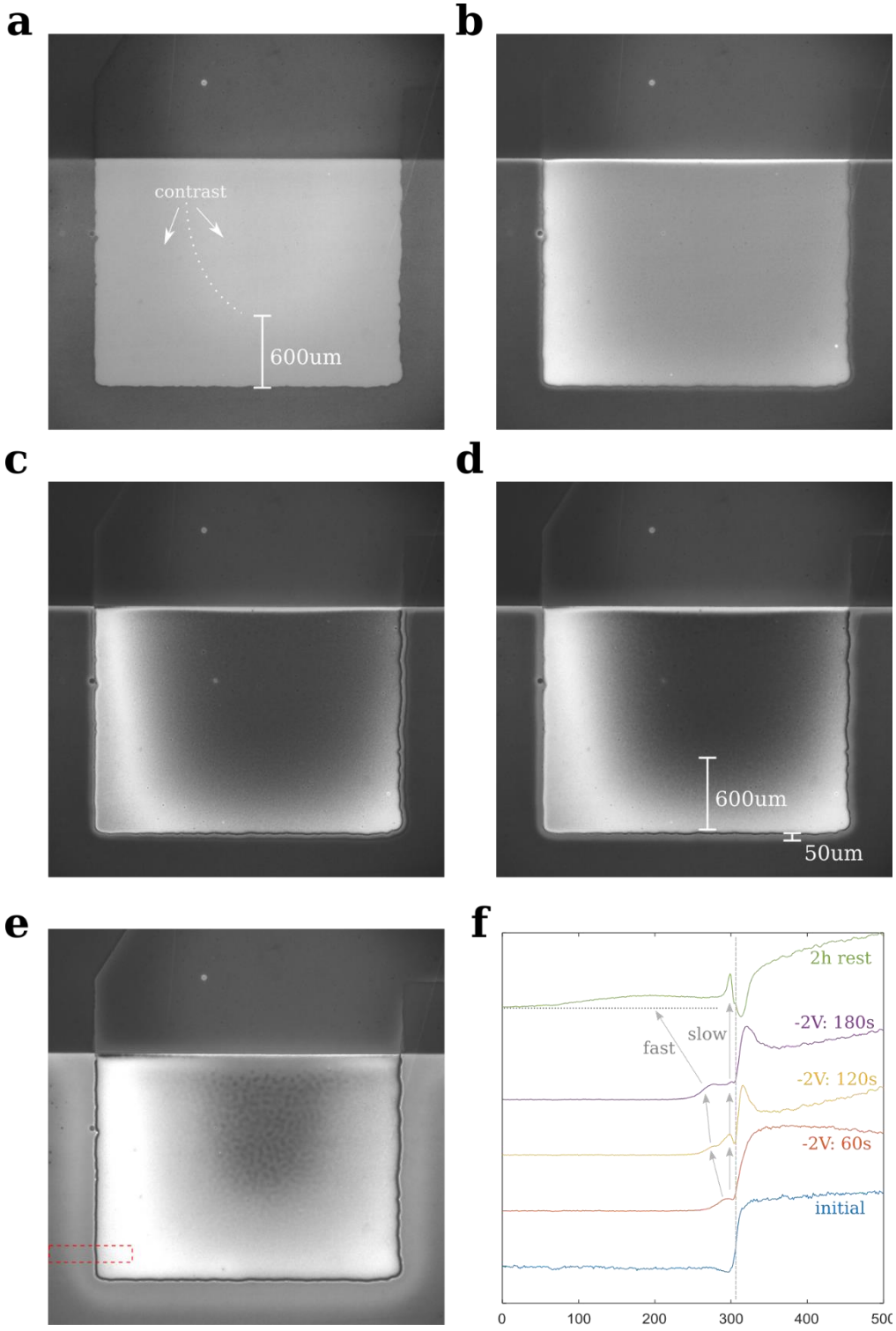

Supplementary Figure 3. Edge effects during short-term reverse-bias testing. Uncropped PL images (γ-adjusted for clarity, γ=0.5) corresponding to the excerpts shown in Fig. 2c-e, taken at various intervals during a test at -2V: (a) initial, (b) after 60s at -2V, (c) 120s, (d) 180s, and (e) after 2 hours in the resting state. Images were acquired in open-circuit condition. Note that the large-scale variation across the active area, easily visible in (b)-(e), is actually present in the initial image (a). As the devices were kept in an N_2-filled glovebox for ~3 weeks prior to these tests, we suspect that these patterns represent lateral migration under the built-in field (the fact that these features follow the Ag-boundary may suggest p-doping in the perovskite, see the discussion of Fig. 6 in the main text). (f) Line-averages (distance in μm) taken from the red-boxed region in (e), showing the propagation of a fast species which extends more than 200μm from the edge after the 2h rest, as well as shorter-range (<30μm) relaxation near the edge over the same time period, suggesting the presence of multiple mobile species.

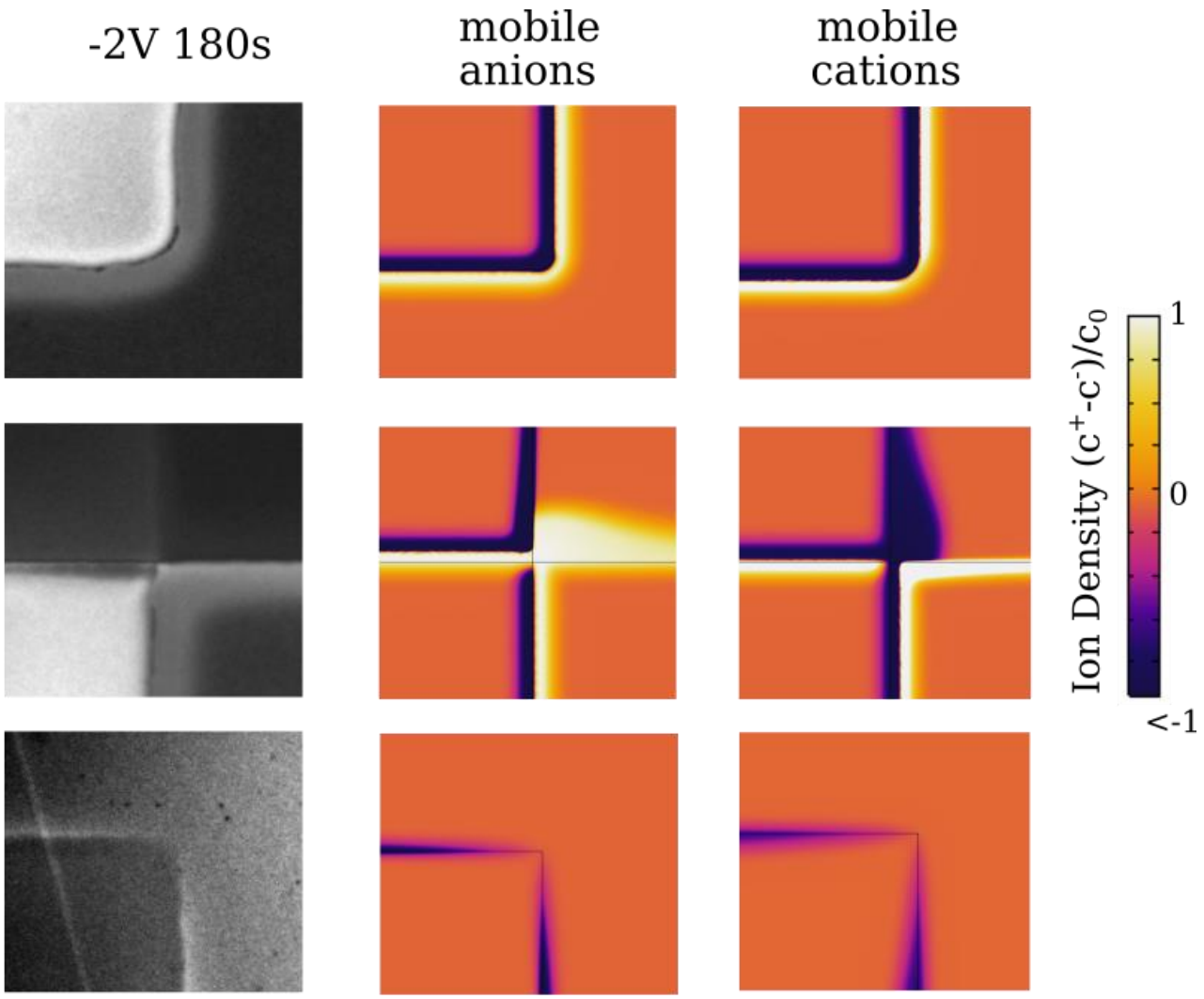

Supplementary Figure 4. Anion versus cation ion migration. Regions of interest in the experiment of Fig. 2 shown with simulations in which either anions or cations are made mobile (the other species acting as a fixed space charge).

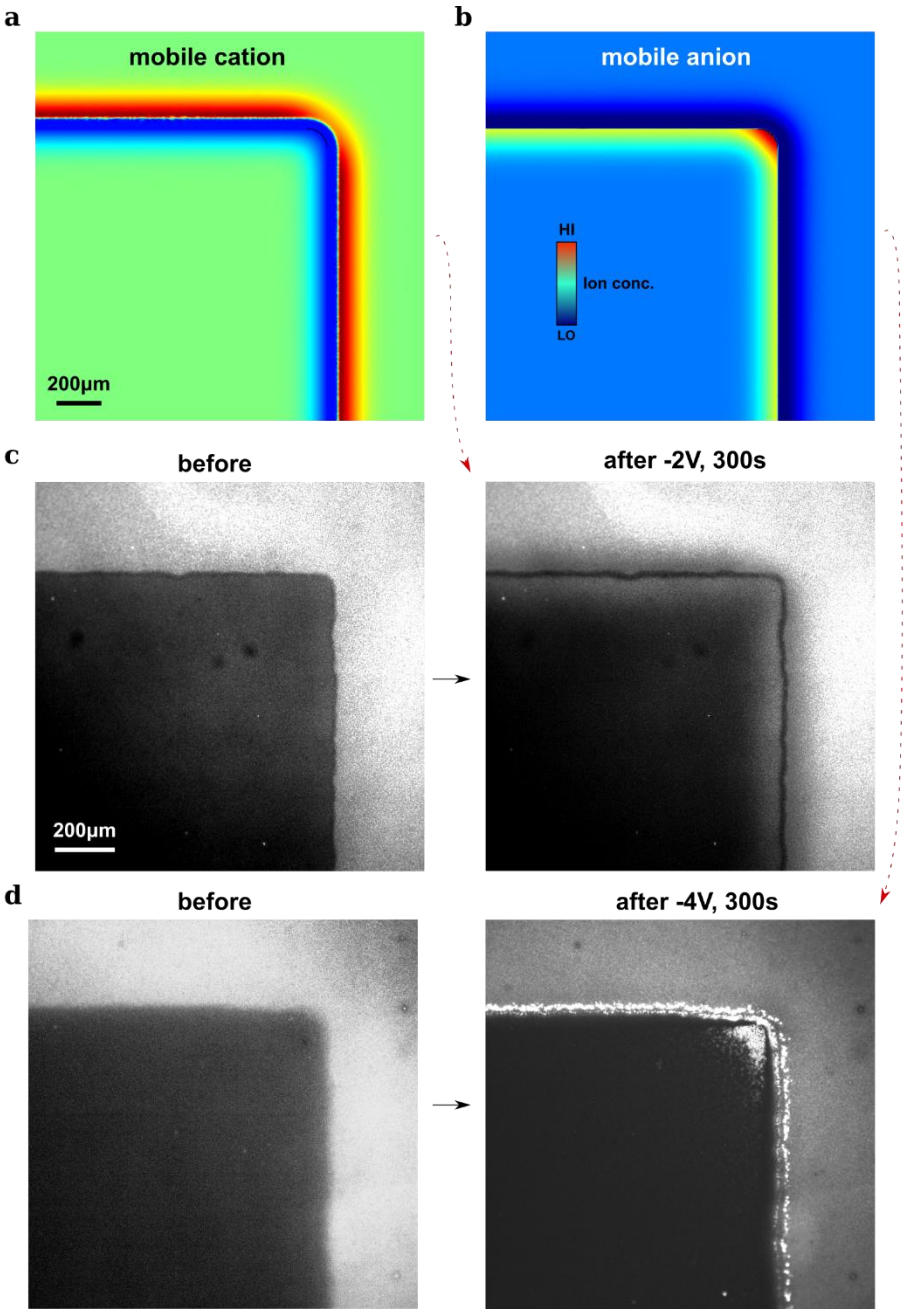

Supplementary Figure 5. Anion versus cation migration. (a,b) Simulation of lateral ion migration under reverse bias (-4V) around a cell corner with positive (a) and negative (b) test charges. Positive charges are expelled, and negative charges attracted into the active area under reverse bias. The different patterns in (a) and (b), especially around the cell corner, can be understood as representing the asymmetry between accumulation and depletion: whereas depletion reaches its limit when the ion in question reaches concentrations near 0, there is no upper limit to the amount of accumulation that may occur (within the assumptions of these calculations). The strong accumulation of anions at the corner due to the convergence of field lines there is therefore not reflected in the pattern of cation depletion. (c) PL images showing a solar cell device before and after reverse-biasing at -2V under nitrogen atmosphere. The pattern of intensity variations most closely resembles patterns of cation migration (in which the positive charge is expelled from the active area under reverse-bias). (d) PL images of a similar solar cell biased at a larger reverse voltage of -4V and subsequently exposed to air. Intense brightening at the cell corner, and a rectangular rather than curved front around the electrode boundary, together give a closer resemblance to expected patterns

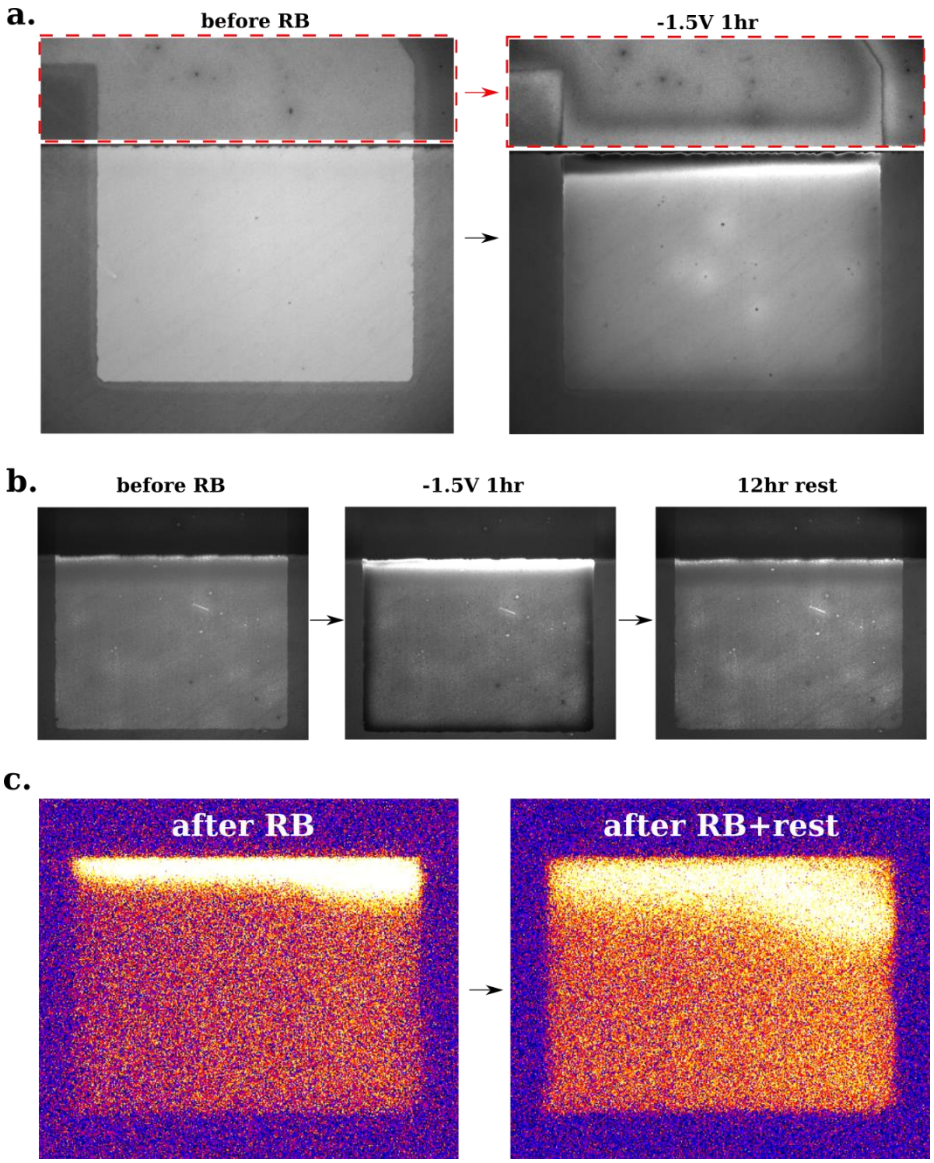

Supplementary Figure 6. Edge effects under reverse bias. (a) A solar-cell device similar to the one shown in Fig. 2 and Supp. Fig. 2, but this time biased for a longer period of 1h at -1.5V. PL modulations are notable in the ITO-free dead-space at the highlighted top of the image (contrast was adjust independently in this region for clarity) as well as inside the active area at the ITO and Ag boundaries. (b) A device imaged immediately before and after reverse-biasing (RB) for 1hr at -1.5V. After 12h rest in storage the PL returned approximately to its initial state. (c) Lock-in thermography images of a solar cell (+1.2V drive) immediately after reverse biasing at -1.5V, and following an overnight resting period, showing enhanced forward current in the region near the ITO boundary which dispersed as a function of time.

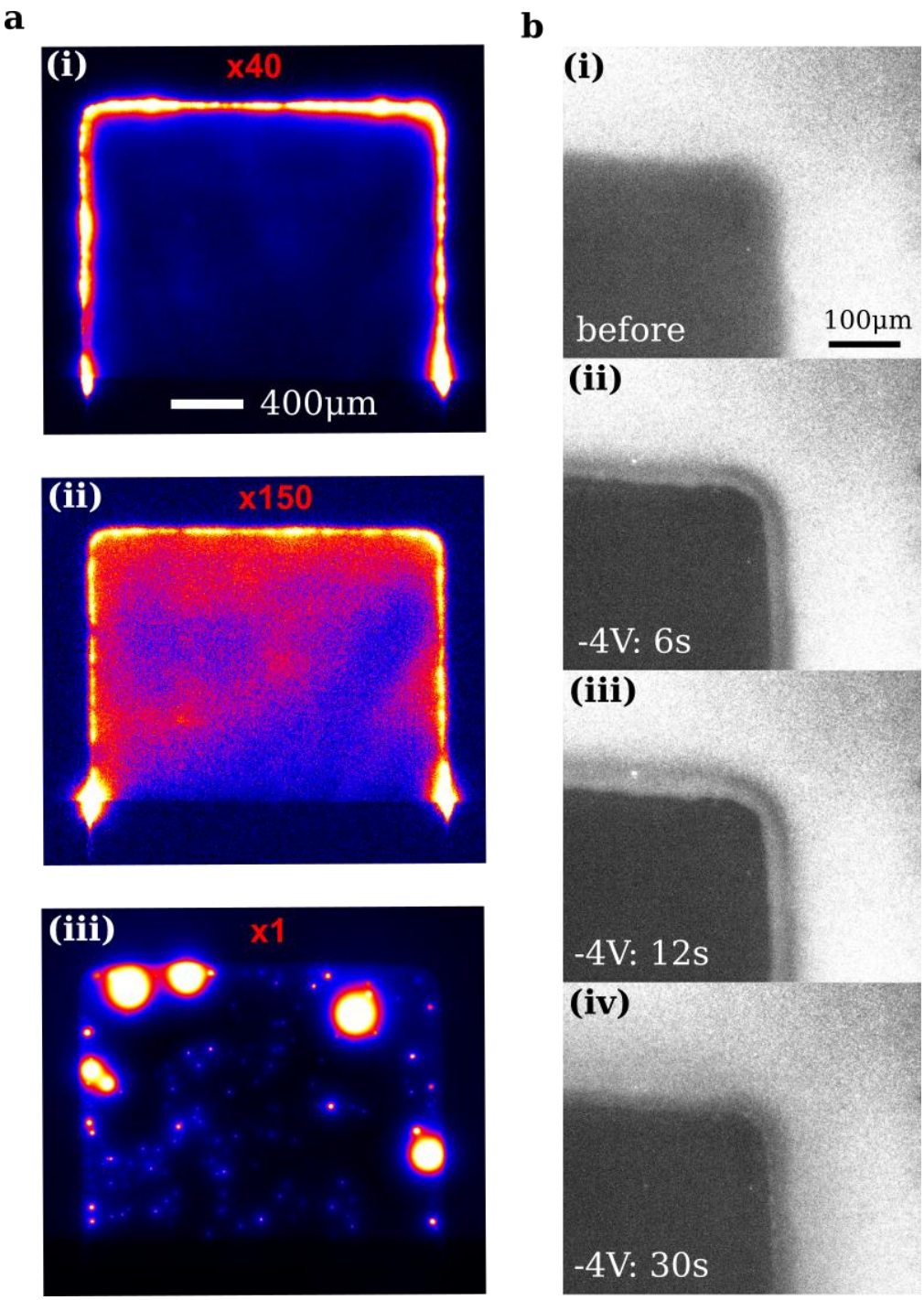

Supplementary Figure 7. Time-series of edge effects during reverse-bias stressing. (a) Sequence of lock-in thermography images acquired at -4V (25Hz), approximately 60s per acquisition, showing current concentration along the active area boundary in the first measurement (i), tending to a more uniform distribution in the second acquisition (ii), and finally degenerating to a collection of hotspots (iii). Red labels indicate scaling of the amplitude images relative to the acquisition in (iii). The progression from (i)-(ii) is consistent with a spike in ion concentration at the Ag (n-)boundary, induced by the sudden application of reverse bias. The degeneration to hotspots in (iii) is typical behaviour for these devices under extreme reverse-bias. (b) Time series of photoluminescence images of a thin-electrode solar cell under -4V (conditions otherwise identical to Fig. 2a). The behaviour of the dark front here is more complex than that shown in Fig. 2b, with outward spreading in (i)-(iii) and a collapse in (iv) (while bias was switched on). We hypothesize that this may be related to the large bias voltage (-4V instead of -2V), which is sufficient to induce significant reverse-current in these devices (the current flow being generally negligible at -2V). Non-zero current will affect the electric field at device boundaries depending on the size of the current density and the lateral sheet resistance. Lateral electric fields will therefore inherit the transient nature of these currents (usually large), which may explain the non-monotonic behaviour.

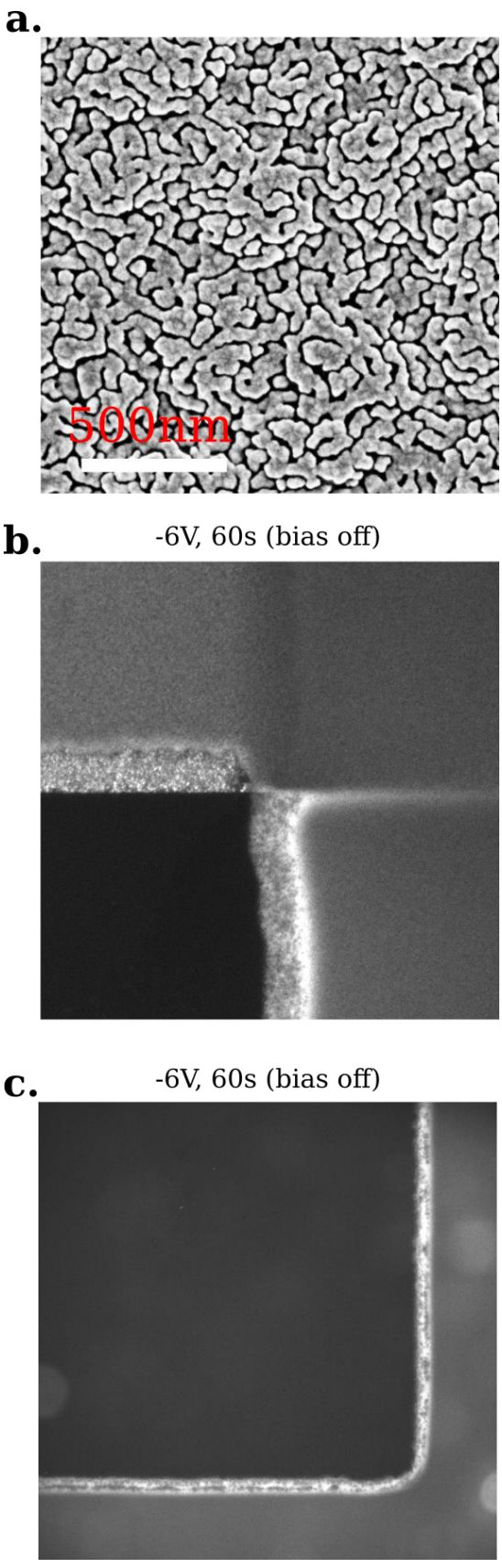

Supplementary Figure 8. Reverse-bias edge effects in thin-electrode devices. (a) Evaporating a thin metal electrode (approximately 15nm on the quartz-crystal monitor) results in a porous but conductive layer that leaves the active area vulnerable to ingress and egress, robbing the metal-electrode boundaries of their special status in that regard (SEM micrograph of thin-Ag surface). (b,c) Results of a harsh reverse-bias test on a thin-electrode device. Activity/damage can be seen at electrode boundaries which resembles the milder patterns in Fig. 2.

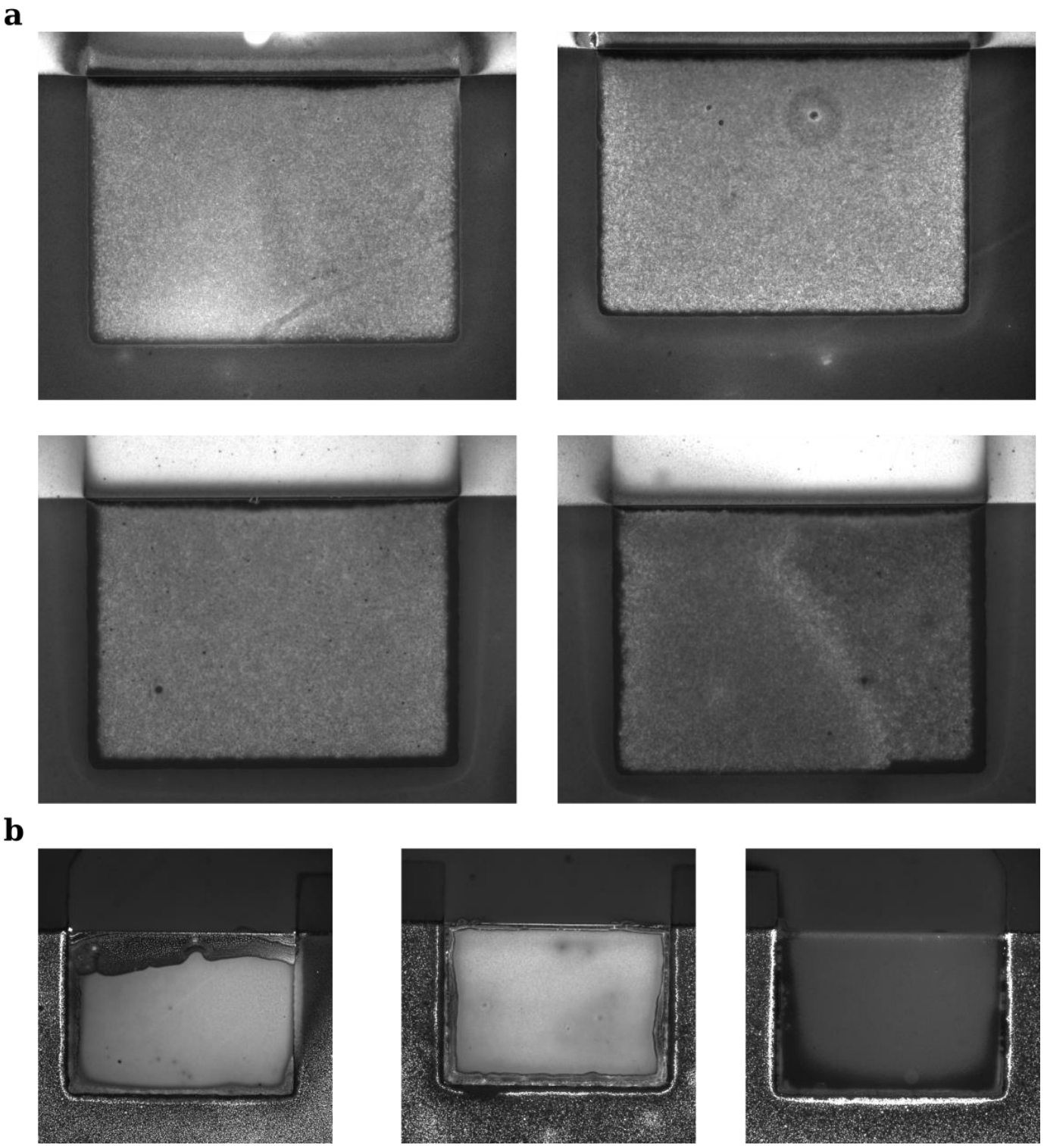

Supplementary Figure 9. Edge degradation during MPP tracking. (a) PL images of solar cells after 100h MPP tracking under AM1.5G, temperature estimated 40-50˚C). (b) Another batch of solar cells aged for only 25h at MPP, but during which the temperature control failed. Edge degradation in this case was severe and accompanied by changes throughout the substrate.

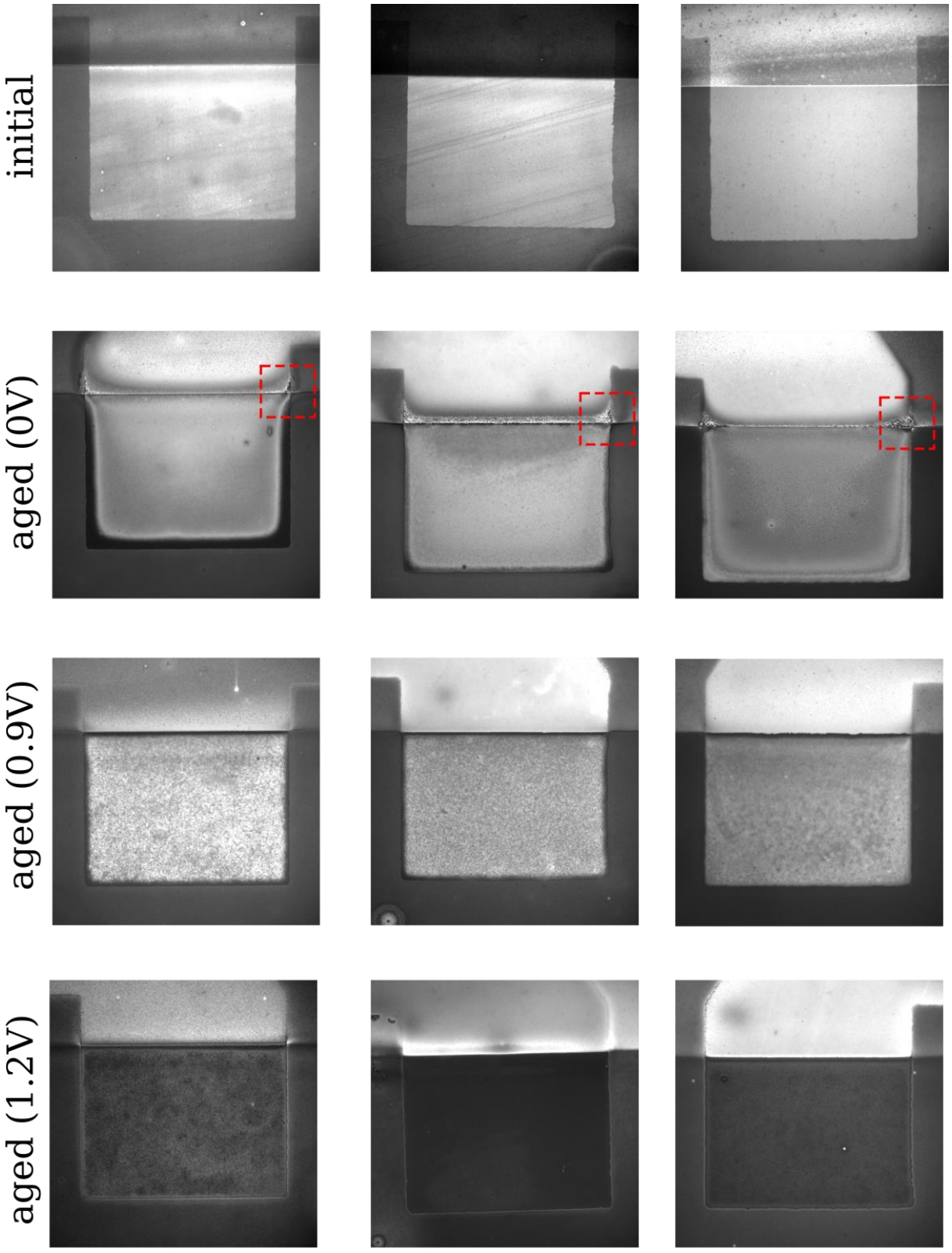

Supplementary Figure 10. Edge degradation at fixed voltage (illuminated ~65°C 25h). Solar cell devices aged under AM1.5G at fixed voltage and elevated temperature, as in Fig. 3, shown at an early stage in the test. Images in the top row show examples of device pixels before placement under the solar simulator. All devices aged at 0V show recognizable patterns at the p-boundary, with strongest degradation in the red highlighted region, as discussed in the main text.

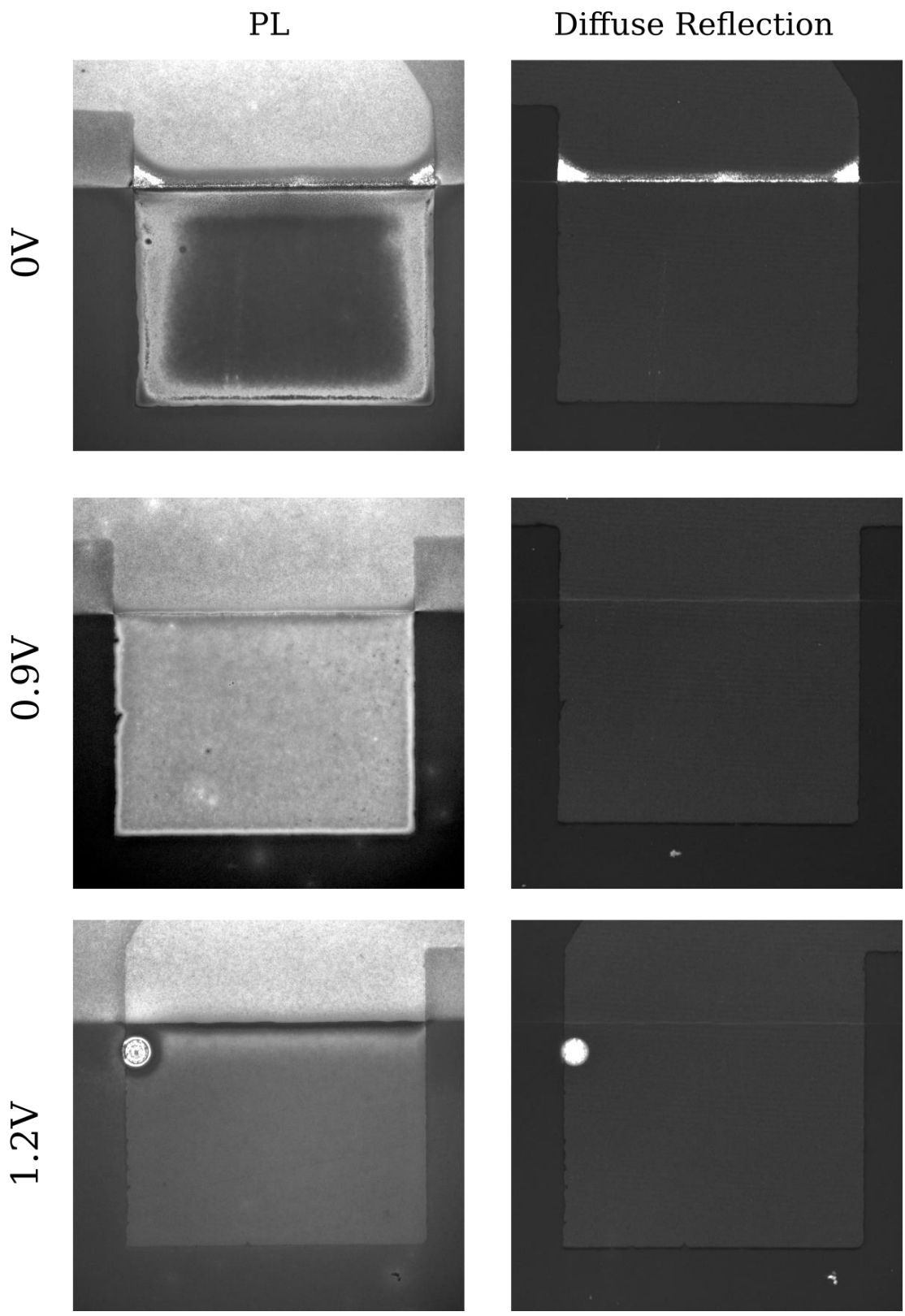

Supplementary Figure 11. Edge degradation at fixed voltage (illuminated, 40°C 180h). Solar cell devices aged under AM1.5G at fixed voltage and a lower temperature of 40°C (as opposed to the aging at 65°C in Fig. 3 and Supp. Fig. 10), shown after 180h of testing. Images on the left show the 672-712nm PL and diffuse reflection is shown on the right. The circular flare in the device at 1.2V indicates a contaminant particle. We note that the dark front around this particle resembles that around the ITO-edge in what appears to be another example of the correspondence discussed in the main text (Fig. 5).

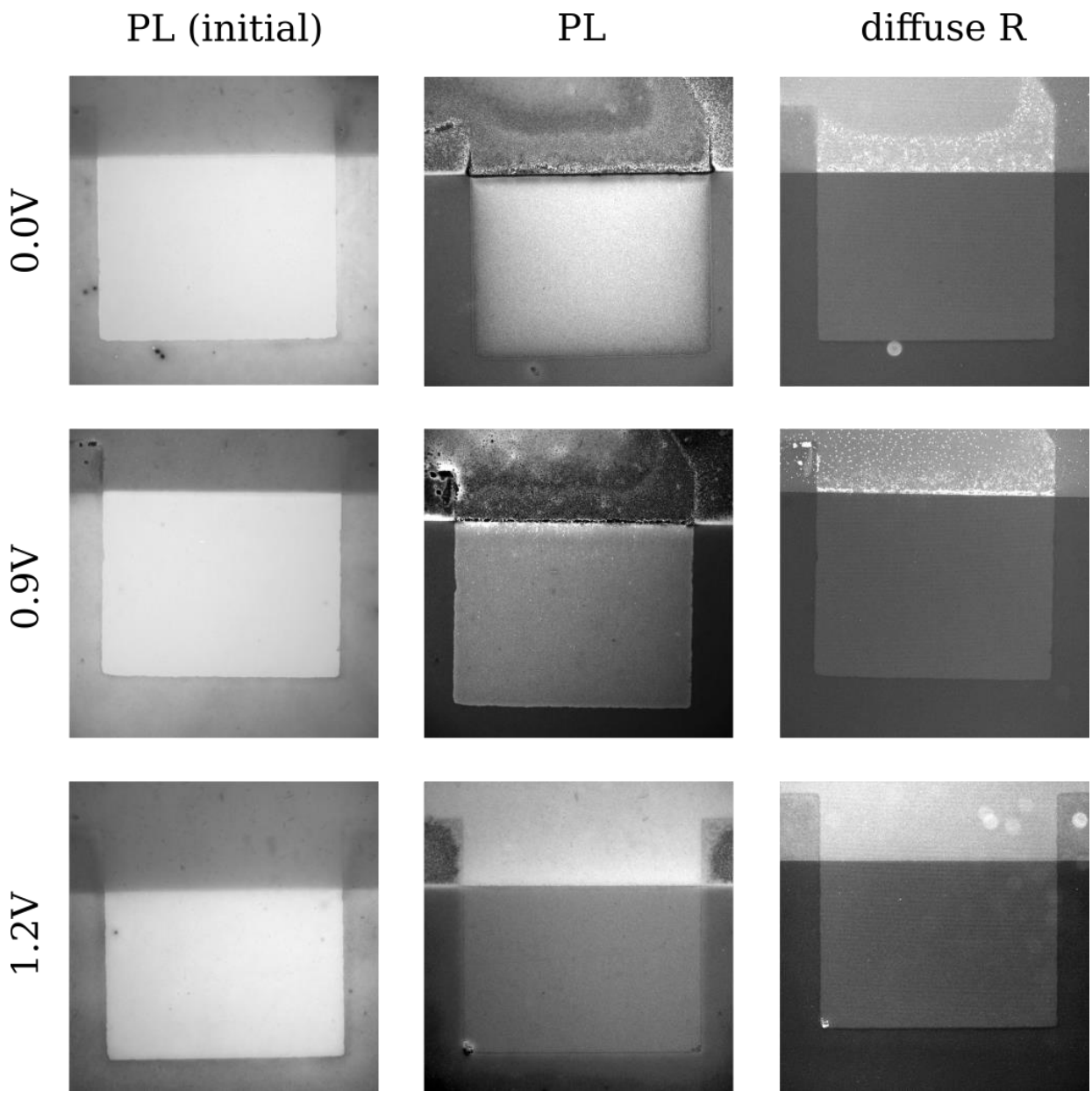

Supplementary Figure 12. Edge degradation at fixed voltage (triple cation one-step absorbers; illuminated, ~65°C 65h). Solar cells processed and aged identically to those in Fig. 3 of the main text (and Supp. Figs. 9-11), but with triple cation absorbers prepared using a one-step method instead of our baseline hybrid CsFA perovskite. The patterns and voltage dependence of degradation at the ITO boundary are the same as those seen with the CsFA devices. It is interesting to note the appearance of early degradation at the bottom Ag corner in the device held at 1.2V – as discussed in the main text and with Supp. Fig. 4 this is a characteristic pattern for ions moving *into* the active area from the dead-space.

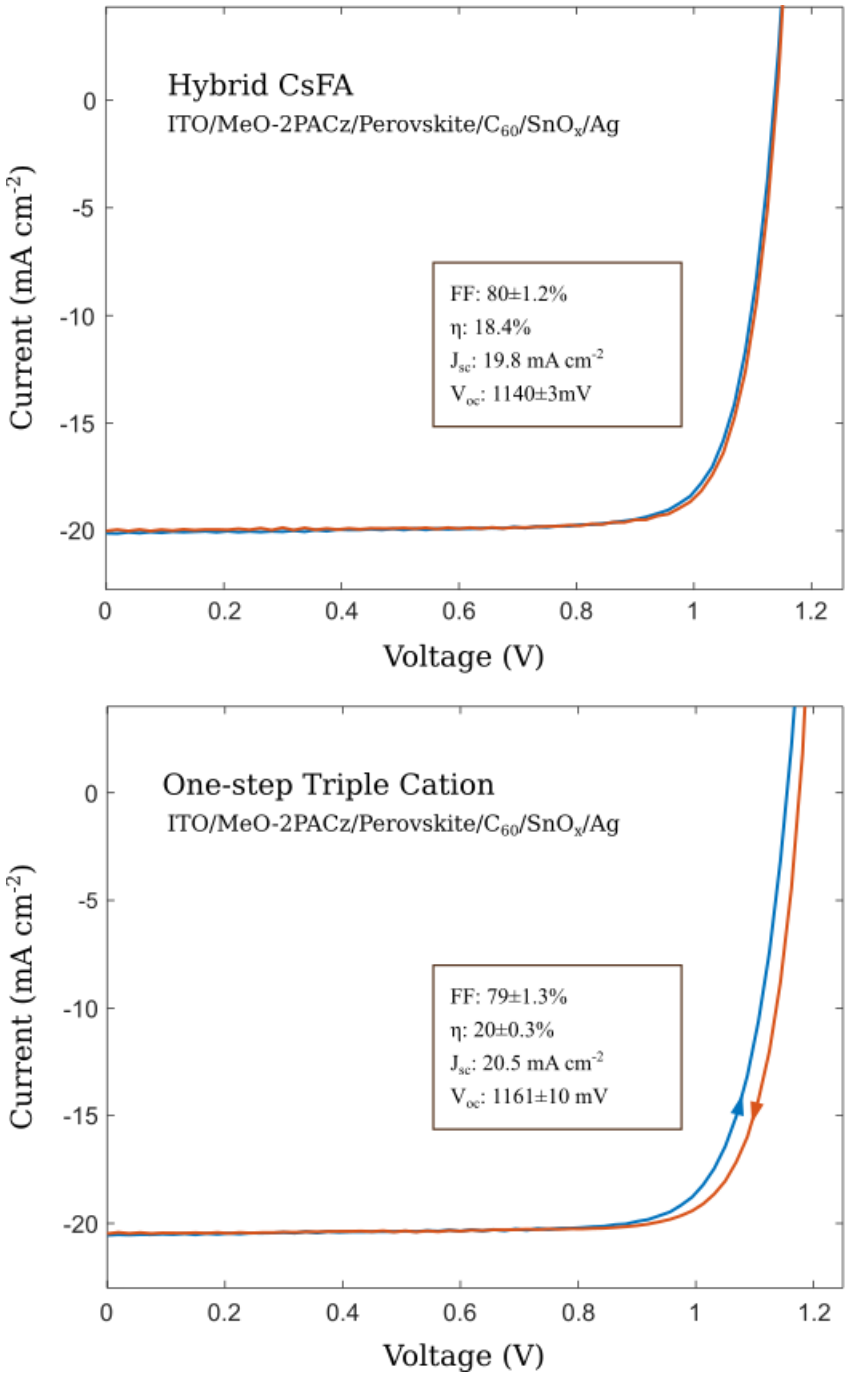

Supplementary Figure 13. IV curves. Representative IV curves for the solar cells reported in the text. (Top) Hybrid CsFA cell – this device features in Fig. 3c of the main text and Supp. Fig. 10. (Bottom) One-step triple cation cell – this device features in the test of Supp. Fig. 12. Fabrication details are provided in the methods section of the main text.

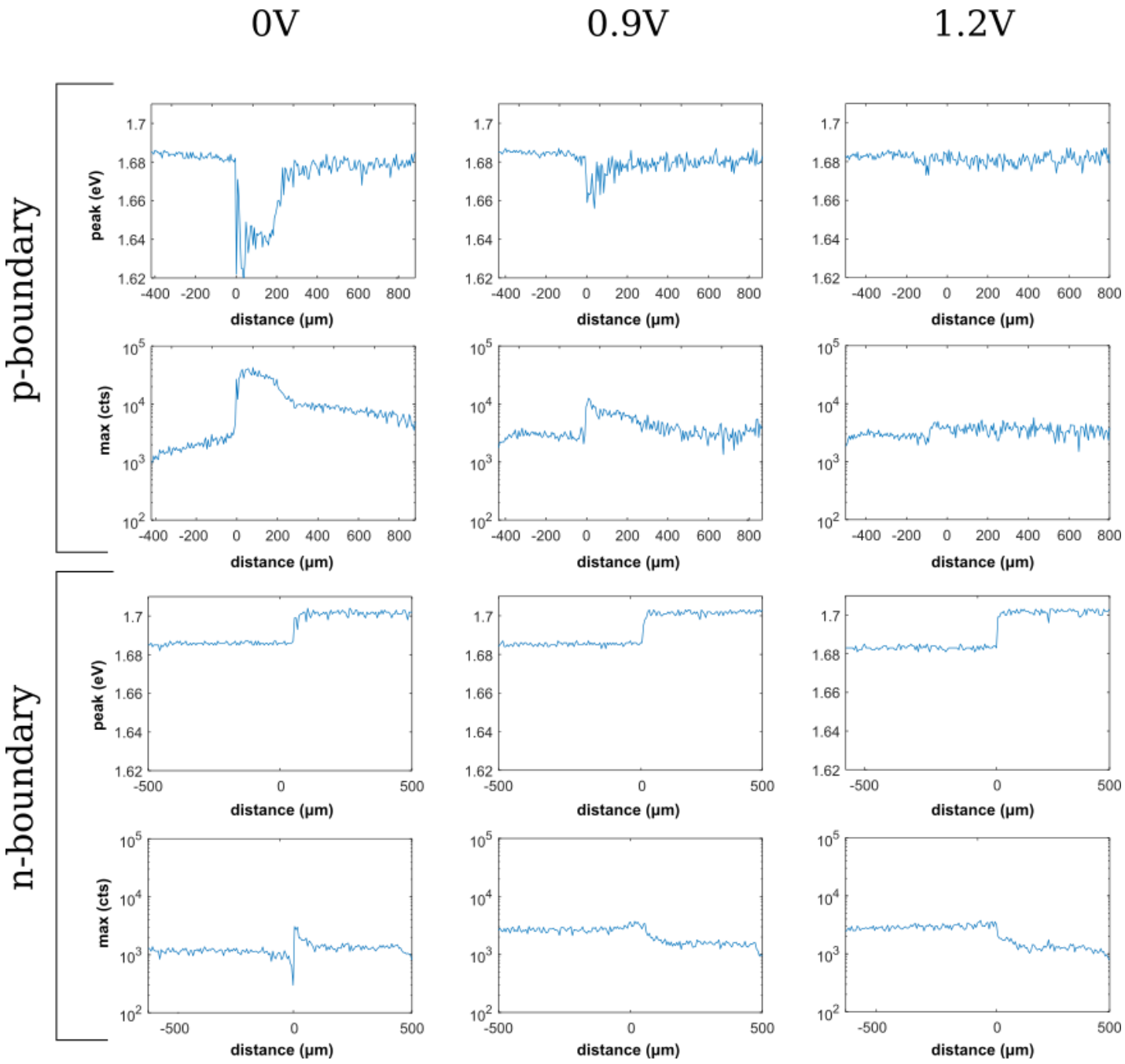

Supplementary Figure 14. PL (spectral) line-scans on devices aged at fixed voltage (illuminated, 65°C 25hr) taken across the p- and n-boundaries. Quantities derived from line-scans in a confocal PL microscope of the devices aged for 25hr at 65°C as a function of voltage. Distance from the respective boundary is shown in the abscissa (active-area towards the negative side).

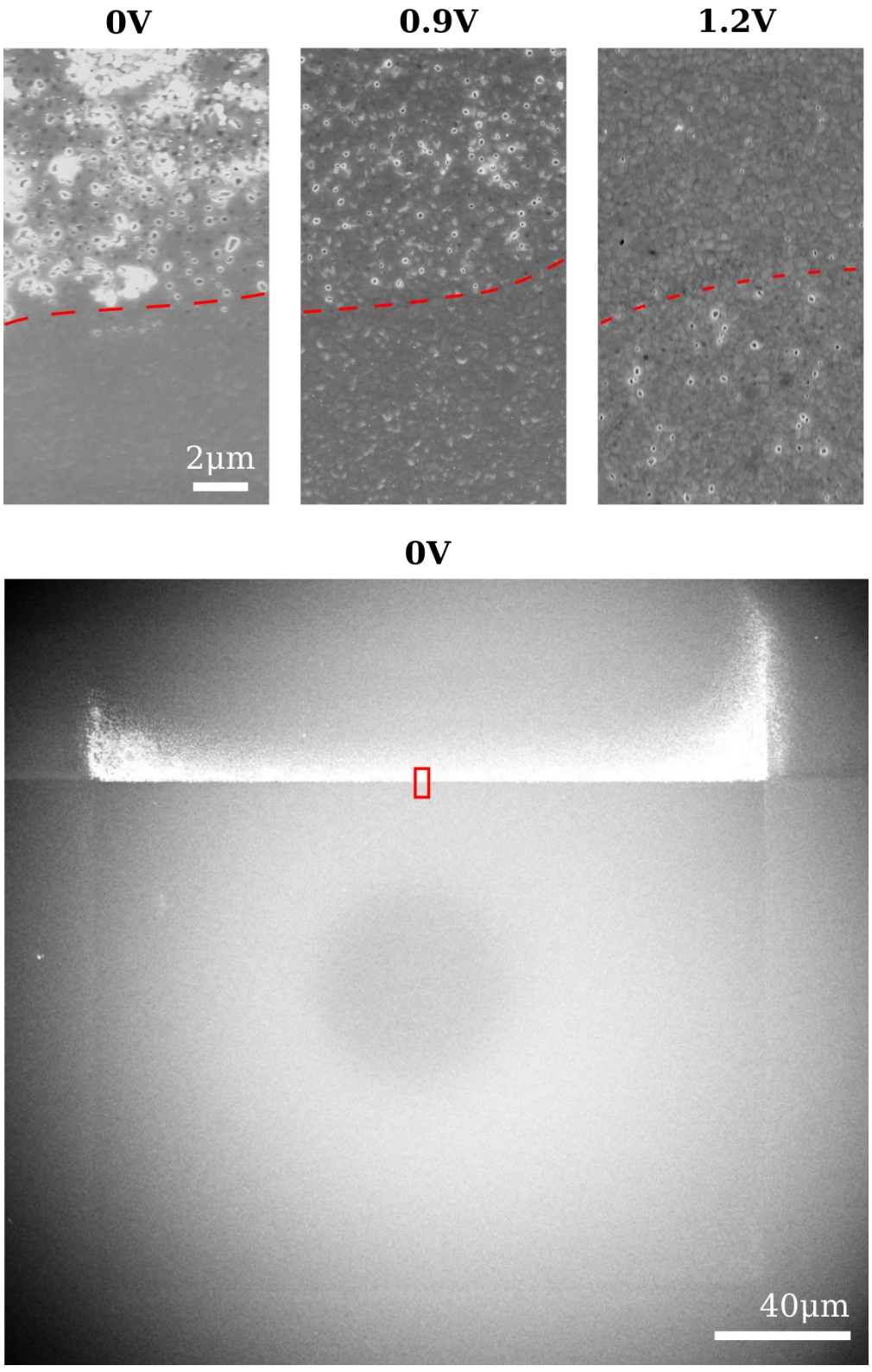

Supplementary Figure 15. Edge degradation at fixed voltage (illuminated). (Top) Portions of the SEM micrographs used to quantify the void density in Fig. 4 (the full images are provided separately as supporting information, and were used to quantify the void density in each region by visual identification and counting). Shown is the top surface of the perovskite film after peeling the top electrode stack (C_{60}/SnO_x/Ag). The region shown is at the ITO boundary (highlighted in red), as shown in the image below. The active area appears at the bottom side.

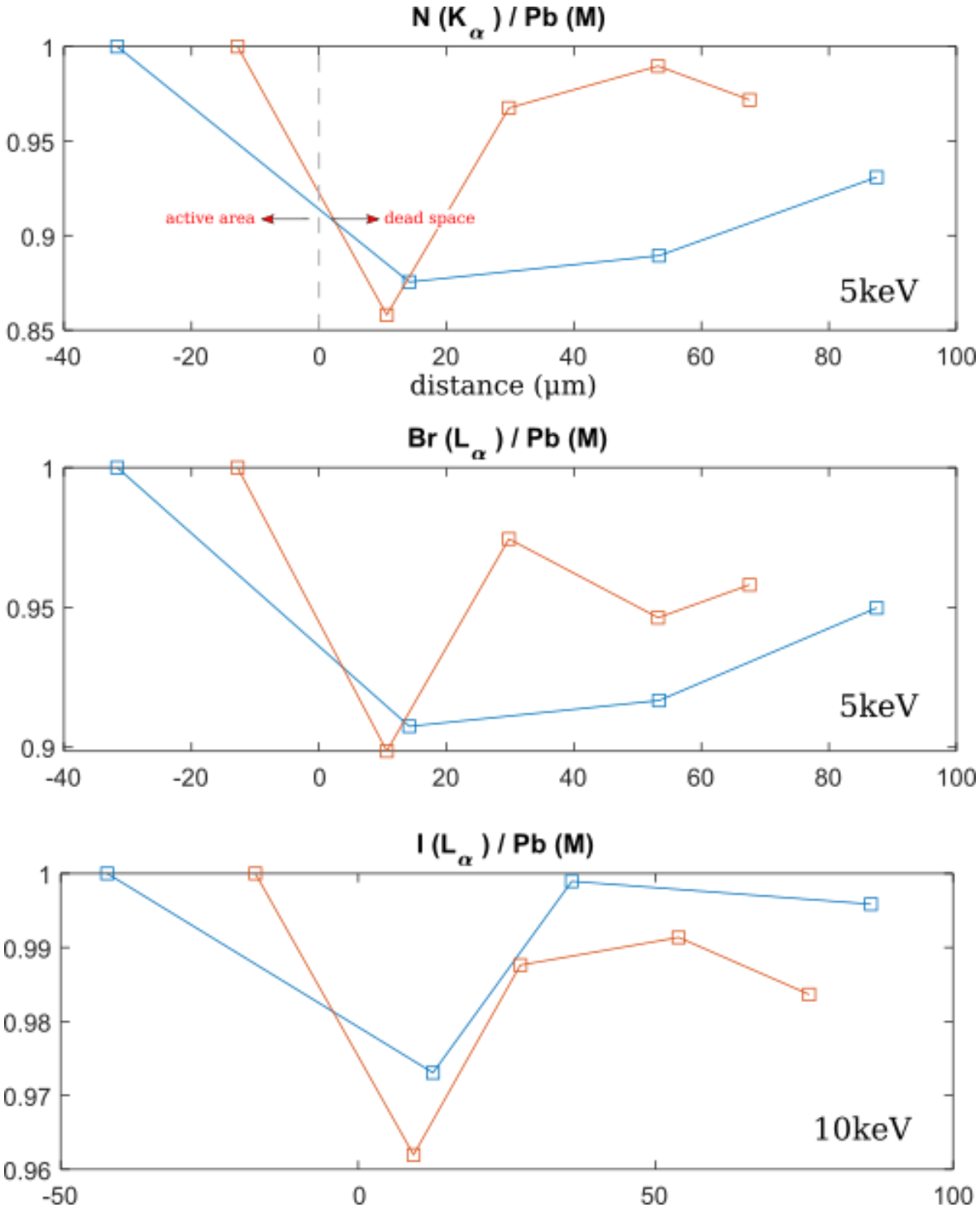

Supplementary Figure 16. SEM EDX at the ITO (p-boundary). EDX line-scans of the 0V device featured in Fig. 4 and Supp. Fig. 13 as a function of distance in µm from the boundary (active area towards the left side). We note a detectable loss of Br, N and I. Some of the missing material was detected on the peeled electrode (data not shown).

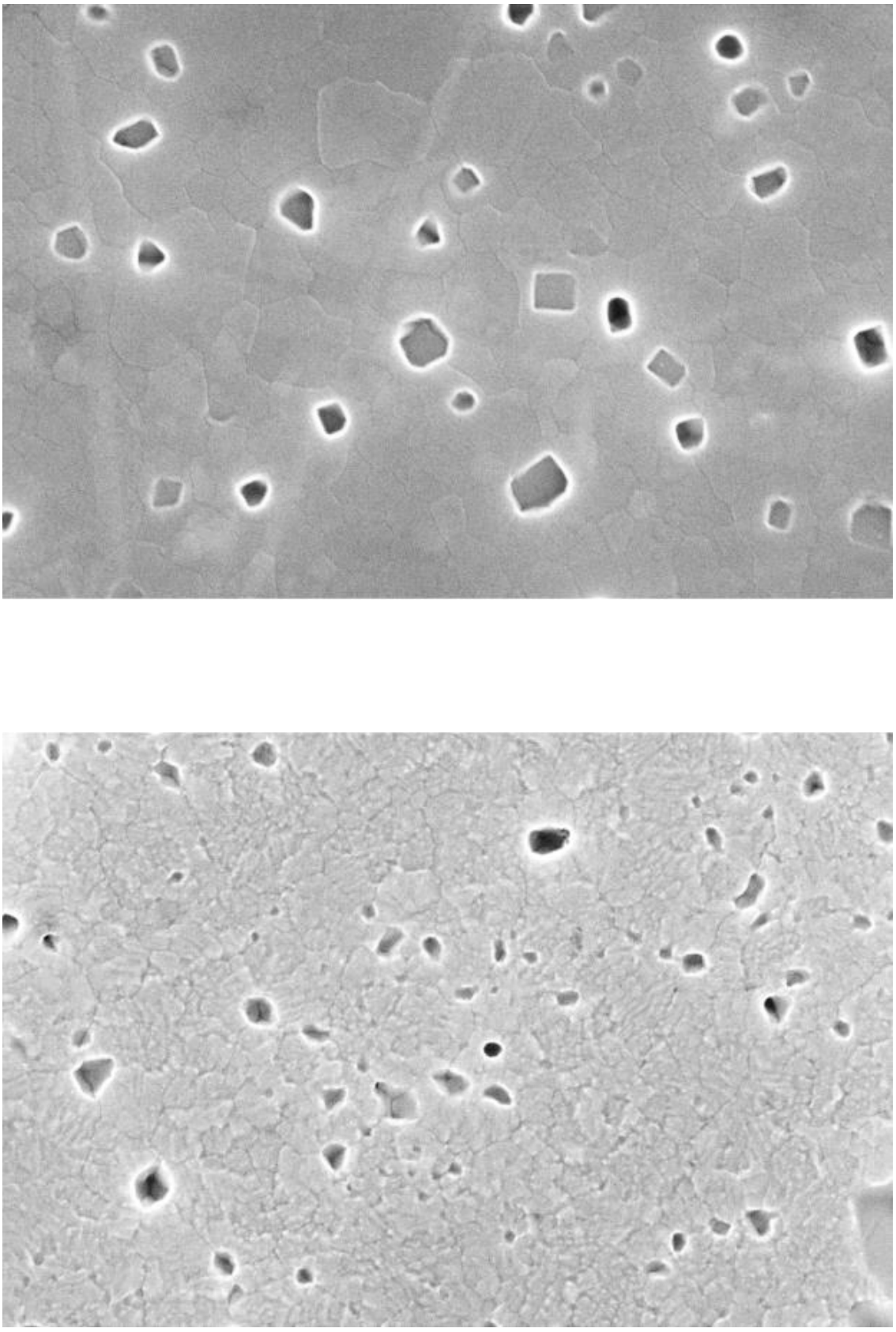

Supplementary Figure 17. Perovskite voids. (top) SEM of a peeled perovskite cell showing voids on the bottom surface of the absorber after aging at 0V in the experiment of Fig. 3. The depicted area was located in the ITO-free dead-space of the solar cell adjacent to the active area (degraded region in Fig. 4a). (bottom) Similar view looking at the active-area of a perovskite cell subjected to -5V for 30s. The apparent roughness of the perovskite surface in the bottom image is an imprint of our ITO's native surface texture, which may also account for the more irregular shape of the voids as compared to the surface peeled from glass (top) .

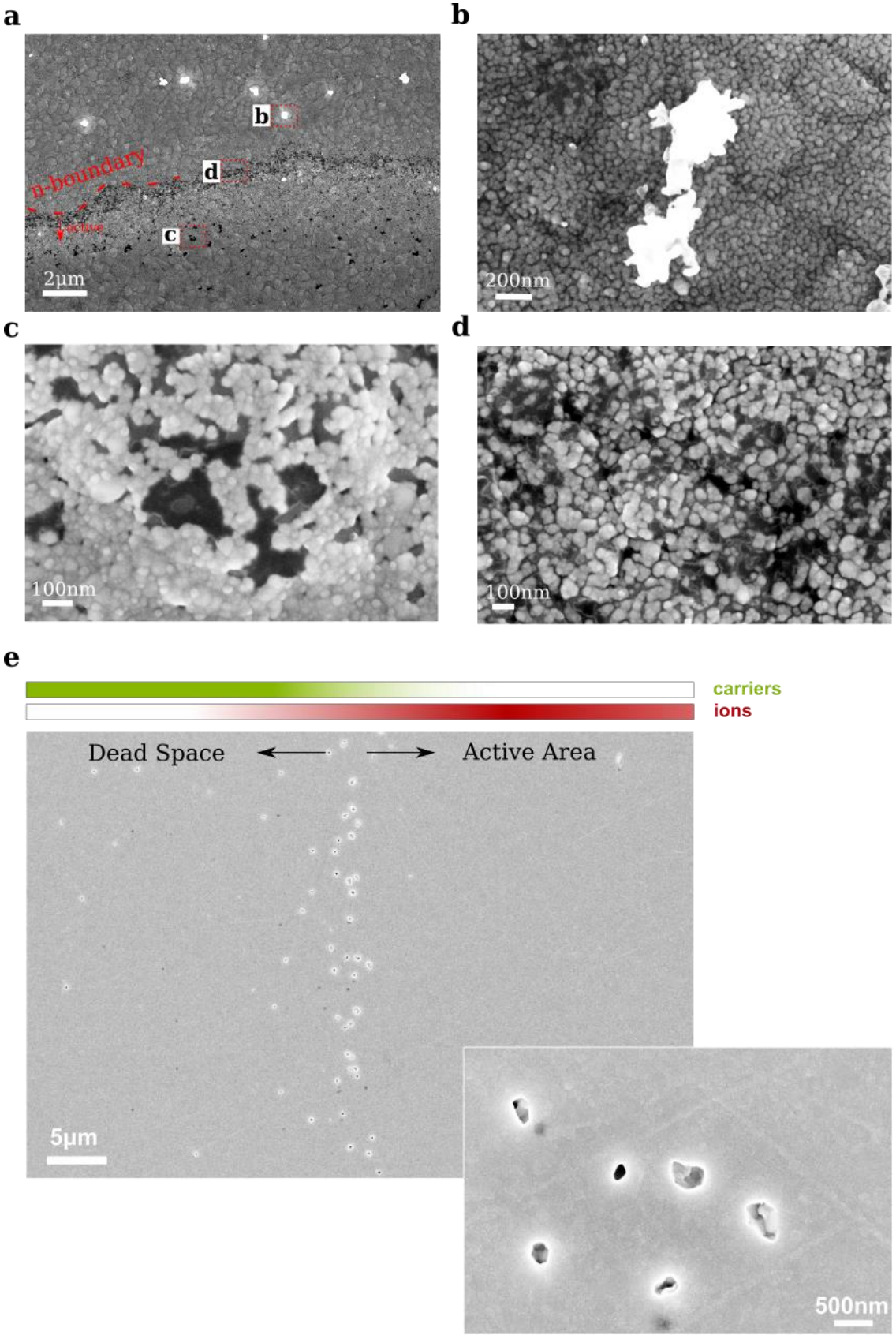

Supplementary Figure 18. N-boundary degradation. Detail of the degradation observed at the n-boundary in devices aged at 0V under illumination, as seen in SEM. (a) Low-magnification of the device top surface (un-peeled) showing several features at the Ag edge, notably: the appearance of Ag agglomerates as shown in (b), and the emergence of an apparently organic substance at the porous Ag boundary (c and d). No such features were found in the bulk of the active area. (e) Low-magnification view of the perovskite film's bottom surface (peeled from the substrate), showing voids as in Supp. Fig. 17. Given the observations and discussion of Fig. 3, we hypothesize that this distribution results from the joint density of carriers and active ions at this interface.

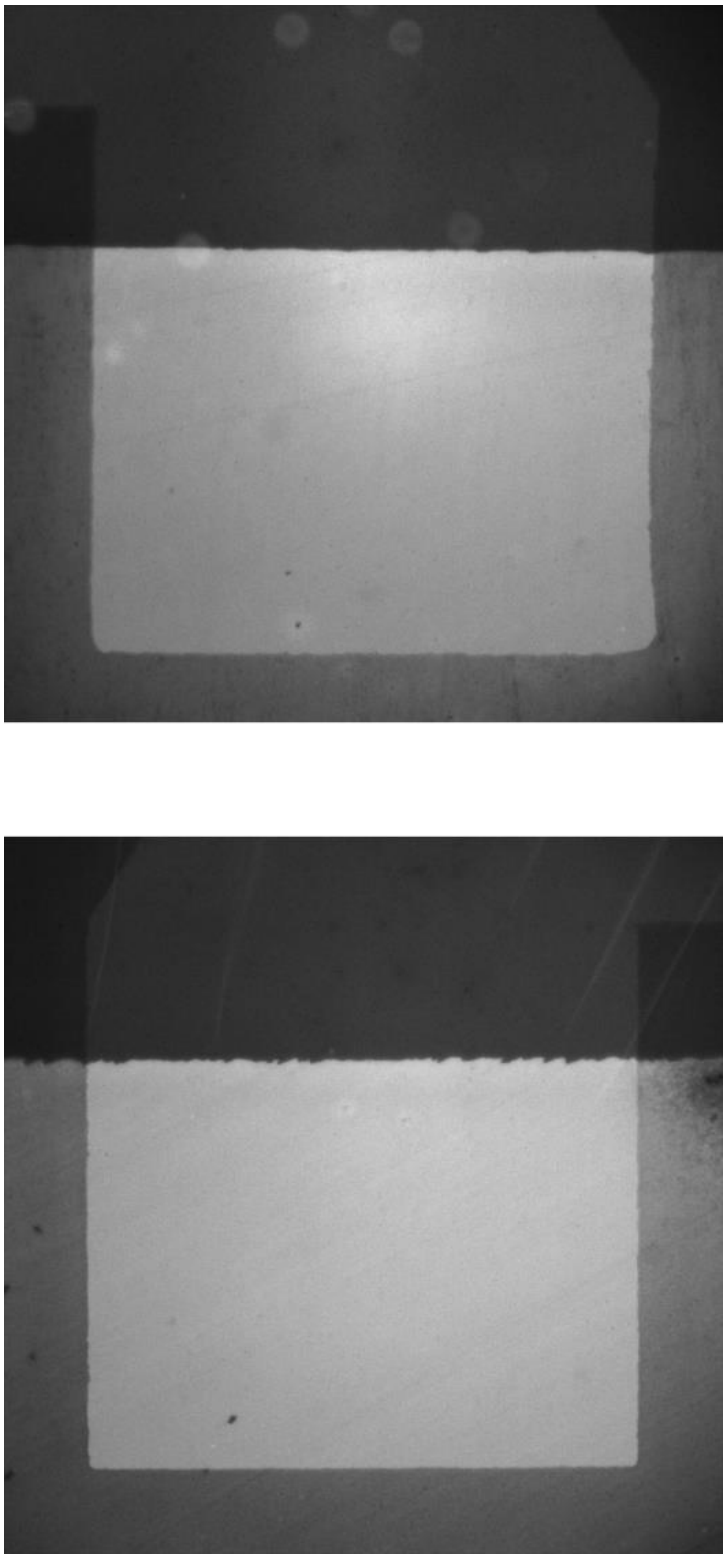

Supplementary Figure 19 . Hot-plate aging. Luminescence images of a solar-cell devices aged at 65°C on a hotplate inside a nitrogen-filled glovebox for 50hr (no illumination). We see no visible PL modulations at the electrode boundaries, in stark contrast to the results of Fig. 3 and Supp. Fig. 7. This suggests that the ionic mechanism of the anodic mode is in some way carrier or light-induced.

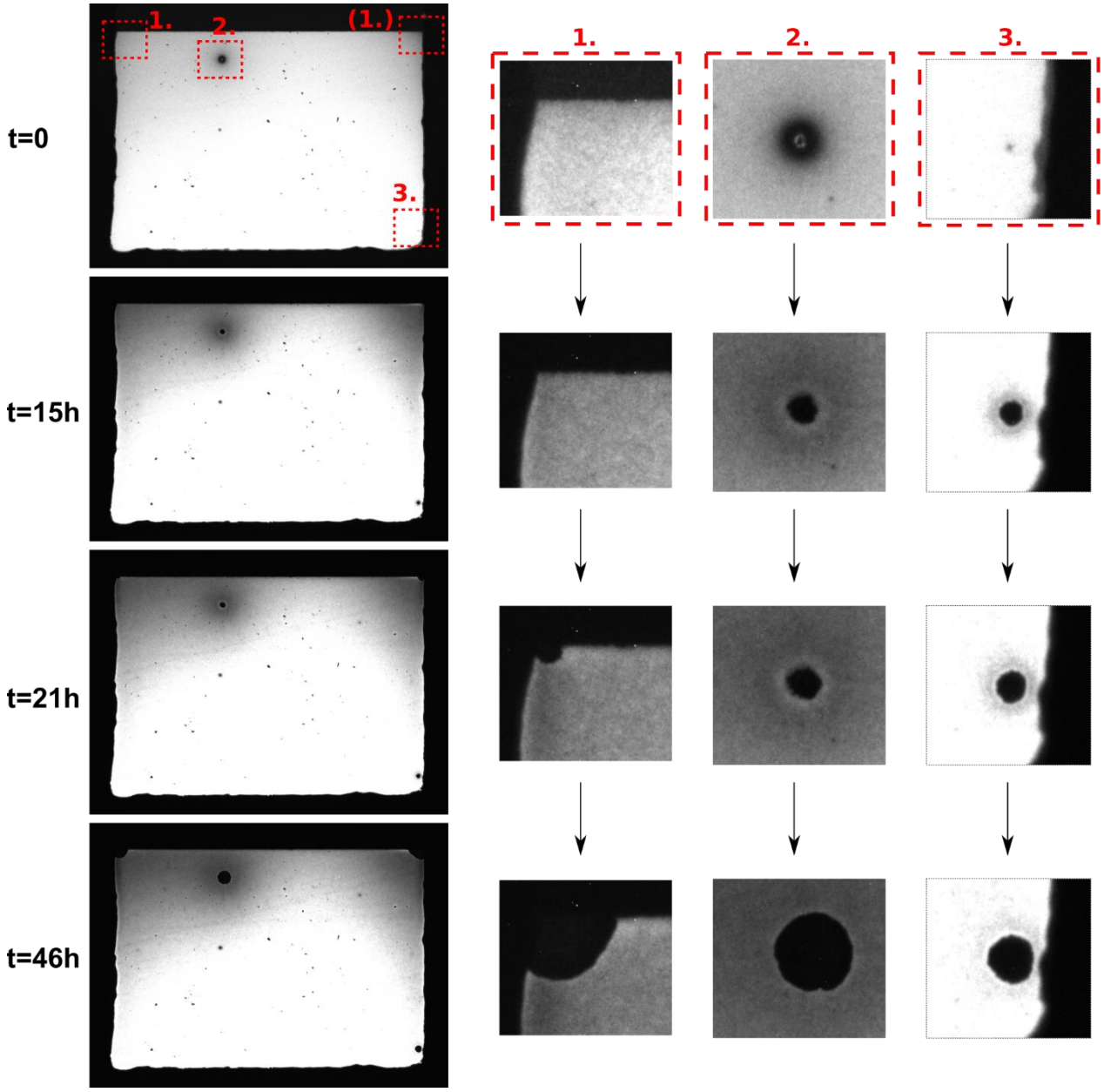

Supplementary Figure 20. Corner degradation in forward bias LED-testing. Luminescence images of a solar-cell device operated in forward-bias (1.3V), i.e. as an LED. Degradation was seen to initiate at four distinct locations after approximately 20h of operation, two being the corners at the intersection of the n-edge and the p-edge (locations labelled 1 and 4 in red), and another two being point defects discernible in the original image (2 and 3). Degradation was seen to propagate at a similar speed and in the same fashion from the point defects and the corners, suggesting a common mechanism. We note also a similarity in the long-range PL modulations around the defect labelled as “2” in the figure and that at the two corners.

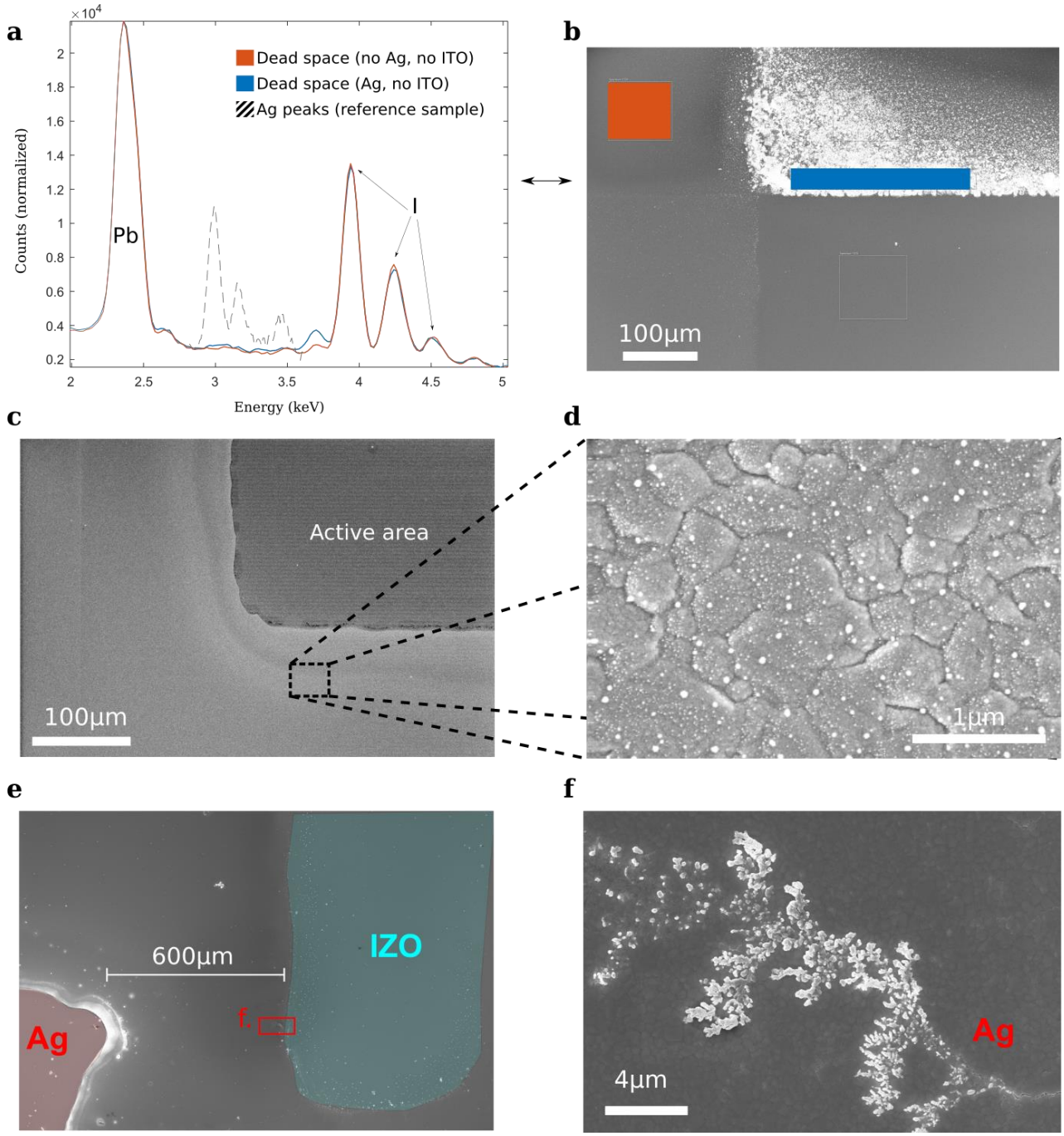

Supplementary Figure 21. Metal migration. (a) SEM EDX spectra for the device of Fig. 4 and Supp. Fig. 15, taken after peeling off the top electrode and contact layers. We show two measurements, one taken in the highly degraded region of ITO-free dead space under the Ag electrode, and one in the dead-space without either electrode, as shown in the SEM top-view image of the peeled device in (b). We find no evidence of Ag migration into the perovskite in either region at levels detectable by EDX. (c) SEM top-view of an MPP-aged device showing "halos" of microscopic Ag particles around the Ag electrode's boundary, as well as a perovskite degradation product emanating onto the top surface (as shown in more detail in Supp. Fig. 18a,c,d). In devices such as these with thick ALD barriers layers between the Ag and perovskite, these halos appear to represent migration of Ag along the top surface, possibly influenced by escaping halides around the degrading boundary. (e,f) SEM top-view images of a lateral test device without any ALD barrier layers (layer stack: glass/perovskite/C_{60}/electrode) and distantly spaced Ag and IZO electrodes. This sample was biased at 10V for 15 minutes on a hot-plate at 120°C. Inspection of the IZO electrode shows dendritic growth of Ag within the perovskite/C_{60} layer (confirmed with EDX), demonstrating lateral field-driven migration of Ag over macroscopic distances (here ~600µm).

Drift-diffusion calculations

Two model types were utilized in the main text to explore aspects of lateral ion migration. These can be respectively described as 2-D "ionic semiconductor" and "diode" models, both of which were developed within COMSOL Multiphysics using the Semiconductor and AC/DC modules respectively.

Ionic semiconductor models (Fig. 1a,b, Supp. Figs. M4-7):

The ionic semiconductor models featuring in Fig. 1, as well as Supp. Figs. M4-7, were made as 2D extensions of 1D models employed previously in the context of I-V hysteresis and electrical impedance spectroscopy [1], [2]. Here we extended those models to include the film thickness plus one lateral dimension. Like their 1D predecessors, these models solve the full set of semiconductor equations for the perovskite stack, here comprising a bottom electrode, the perovskite film, a top-selective contact and the top-side metallization (a monolayer-type HTL is modelled by simply setting a favourable work function and low minority-carrier recombination velocity at the bottom electrode [3]). To this semiconductor model we add a drift-diffusing charge density to model the mobile ions, assuming that ions are localized entirely within the perovskite layer. Parameter values for the models are shown in the tables below.

For the simulations of Fig 1(a,b), a 200 µm domain with logarithmically spaced meshing was used to model an active-area boundary at the edge of the metal (Ag) electrode, with a size of 100 µm either side of the interface:

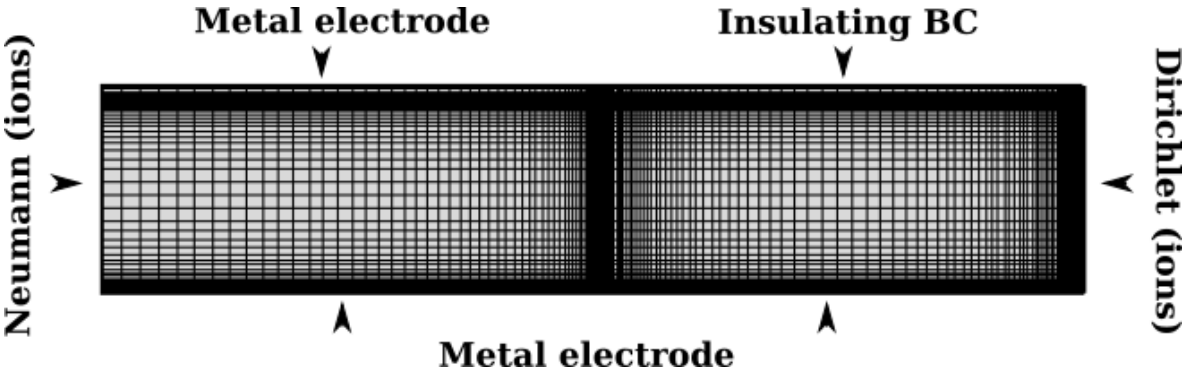

For Supp. Figs. M6-7 an analogous domain was set up to emulate an ITO boundary (instead of the Ag edge).

In Fig. 1(a) of the main paper we show the internal potential solved without the presence of mobile ions, as a means of illustrating the driving force for lateral (and vertical) ion migration. In Fig. 1(b) and Supp. Figs. M4-7, ions are included with a homogeneous initial distribution throughout the perovskite layer, and compensated by a stationary space charge of opposite sign, as is usually assumed in modelling studies [4] (we drop this condition in Supp. Fig. M3). The density in Fig. 1(b) was set to a comparatively low value of 10^{15}cm^{-3} to demonstrate the effect of lateral redistribution. The behaviour of higher ion concentrations is discussed in the main text with reference to Supp. Figs. M1-3 & 6.

For the ionic boundary conditions, a blocking condition was applied at the left-side of the active area, and a Dirichlet condition ($c = c_0$) at the right-side of the dead-space. This means that in these simulations the right-side boundary acts as an infinite source/sink for the ions, a fact which is important in allowing active-area concentrations to greatly exceed their initial value towards equilibrium (Fig. 1b). These models therefore simulate a small active area in contact with a much larger surrounding of dead-space, which is qualitatively appropriate for our small-area solar cells (2 mm x 1.5 mm active areas on 25 mm x 25 mm substrates).

In Supp. Fig. M1-M3 we employ our 1D ionic semiconductor models to illustrate the effects of ionic band-bending at different ion densities, and to check the consistency of our 2D models in Supp. Fig. M4.

Absorber	
ε	50
E_g	1.65 eV
χ	4.0 eV
N_c	1e19 cm^{-3}
N_v	1e19 cm^{-3}
Gen./Recomb.	0*
Ion conc (initial)	1e15-1e18 cm^{-3}
D_{ion}	1e-10-1e-8 cm^2/s
Thickness	400 nm

C_{60}	
ε	3
E_g	2.2 eV
χ	4.2 eV
N_c	1e20 cm^{-3}
N_v	1e20 cm^{-3}
thickness	20 nm

SnO_x	
ε	9
E_g	3.6 eV
χ	4.2 eV
N_c	1e19 cm^{-3}
N_v	1e19 cm^{-3}
thickness	20 nm

Top Electrode	
WF	4.2 eV

Bottom Electrode	
WF	5.4 eV
Recombination velocity (electrons)	1 cm/s

*generation/recombination was added in Supp. Fig. M7 as specified in the figure caption.

2D diode models:

To address our planar observations of solar cell devices (Figs. 2-5, plus examples in the SI) we also developed a simpler class of models, this time in the two lateral substrate dimensions ignoring the film thickness. Our main requirement for these models was that they should capture the qualitative trends outlined in band diagrams of Fig. 1c,d i.e. that they should qualitatively represent the bias-dependence of potentials inside the active area, as well as in the two dead-space zones in contact with only one electrode assuming flat-band conditions. The details of the model mainly affect the "interpolation" of internal potential between these substrate regions, which is of secondary interest for the large-scale patterns of ion migration. These models rely crucially on the application of flat-band conditions within all regions of dead-space: whilst this is an essentially ad-hoc assumption for the analysis of reverse-bias experiments , it is well-justified for the illuminated experiment of Fig. 3c since photo-generated carriers will indeed induce approximately flat bands in all regions of dead-space (no shadow masks were used).

Models were accordingly developed based on the heuristic idea that electrons and holes can be described as moving 2-dimensionally in independent (but coupled) electrical potentials, corresponding to the internal potential at the top (V_{top}) and bottom (V_{bot}) of the perovskite film. Lateral carrier transport was taken to be ohmic with an effective conductivity representing joint transport in the perovskite and electrodes layers (where present). Ohmic transport coupled with generation-recombination in the continuity equation then determines the values of the two potentials. Recombination was taken to follow a diode law in the difference (with generation corresponding to approximately 1-sun intensity)

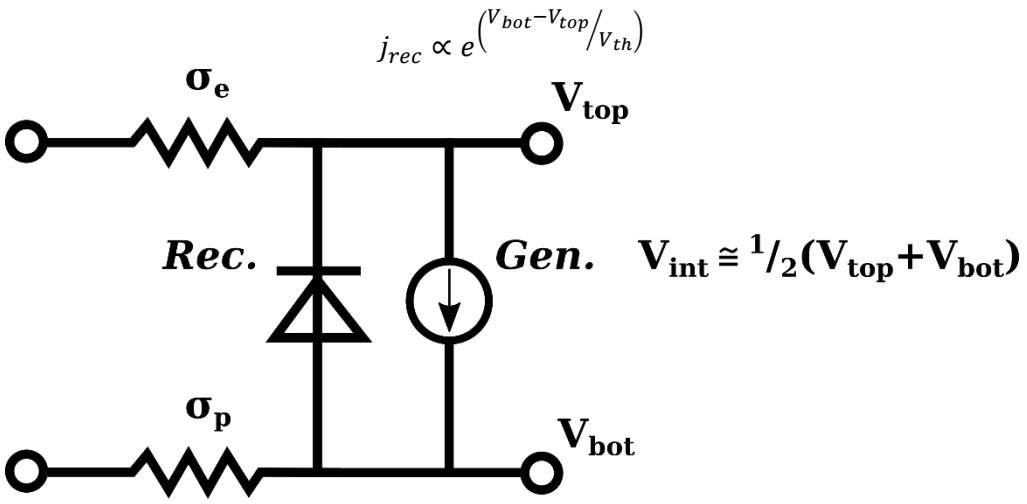

Supplementary Figure M2. Transmission line corresponding to the 2-D diode model used for computing approximate lateral potentials.

This intuition for this model is provided by the fact that, for biases significantly below the built-in voltage at least, carriers will indeed be largely separated across the film thickness by the internal field, and will therefore experience a local potential (weighted by concentration) approximately equal to the values at the top and bottom of the film. We note that this picture begins to break down for applied voltages approaching and exceeding V_{bi}, and will be less accurate in modelling films with a high ion concentration (for which internal fields are largely screened to the interfaces and carrier separation is consequently weaker). The two potentials V_{top} and V_{bot} were determined in COMSOL's AC/DC Electric Currents module, which solves a Laplace equation coupled to Ohm's law $j = \sigma E$ in the lateral carrier current for each potential. In substrate regions covered by ITO we set a high lateral conductivity for the holes (such that V_{bot} is essentially constant over the ITO – we take this value as ground) and likewise in the metallized regions we set a high electron conductivity (such that $V_{top} \approx V_{applied}$). Elsewhere we set low but essentially arbitrary values for the carrier conductivities: the exact values only affect the lateral spread of applied potential from each electrode. Values were chosen such that potentials drop within a few 10s of microns from each electrode, which corresponds approximately to patterns of electroluminescence in our devices. The value chosen (10^{-9} S) is also the conductivity corresponding to a carrier density of approx. 10^{13} cm^{-3} with μ=10 cm^{2}V^{-1}s^{-1} ($\sigma = e\mu_n n \; or \; e\mu_p p$), values which are not unrealistic under 1-sun illumination. We note that the flat-band condition is not built-in but emerges in these models as in dead-space far from the electrodes $j_{gen} = j_{rec}$ (lateral transport being negligible), and consequently $V_{bot} \approx V_{top}$, which is a statement of the flat-band condition.

Active area	
σ_n	10^2 S
σ_p	10^2 S

Dead space (ITO only)	
σ_n	10^{-9} S
σ_p	10^2 S

Dead space (Ag only)	
σ_n	10^2 S
σ_p	10^{-9} S

Once computed, lateral potentials were used to provide the drift term in 2D drift-diffusion models of ion migration. For the drift field we simply used the average potential $\frac{1}{2}\left(V_{bot} + V_{top}\right)$.

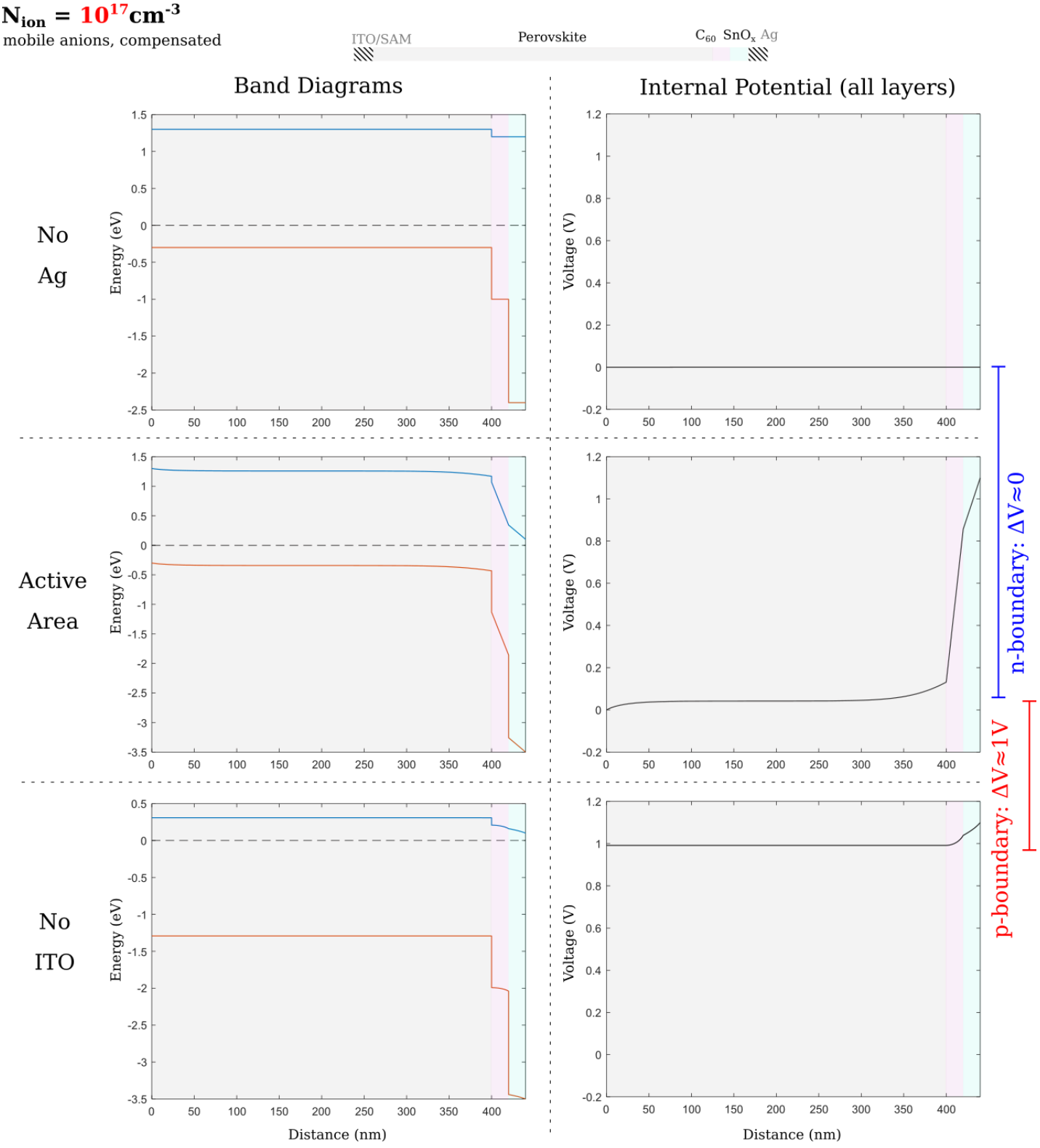

Supplementary Figure M1. 1D drift-diffusion calculations of steady-state band-diagrams (left column) and internal potential (right column) for a moderately high ion density of 10^{17}cm^{-3}. A colour code for the layer stack is sketched at the top of the figure. The ITO and Ag electrodes are taken to be at equipotential (0V applied bias). Inside the active area (middle row) the ion density is sufficient to screen most of the electric field within the perovskite, causing potential drops within the C_{60}/SnO_x bilayer instead. In consequence, the average internal potential inside the perovskite layer hardly varies at the n-boundary (Ag-interface) as shown on the right, whilst there is a large lateral difference of ≈1V at the p- (ITO-) boundary. To be compared with Supp. Fig. M2. We note that there is a trade-off between amount of potential dropped at the n- and p-boundaries since the two potentials must add up to the difference in vacuum potential between the two electrodes (V_{bi}-V_{app}).

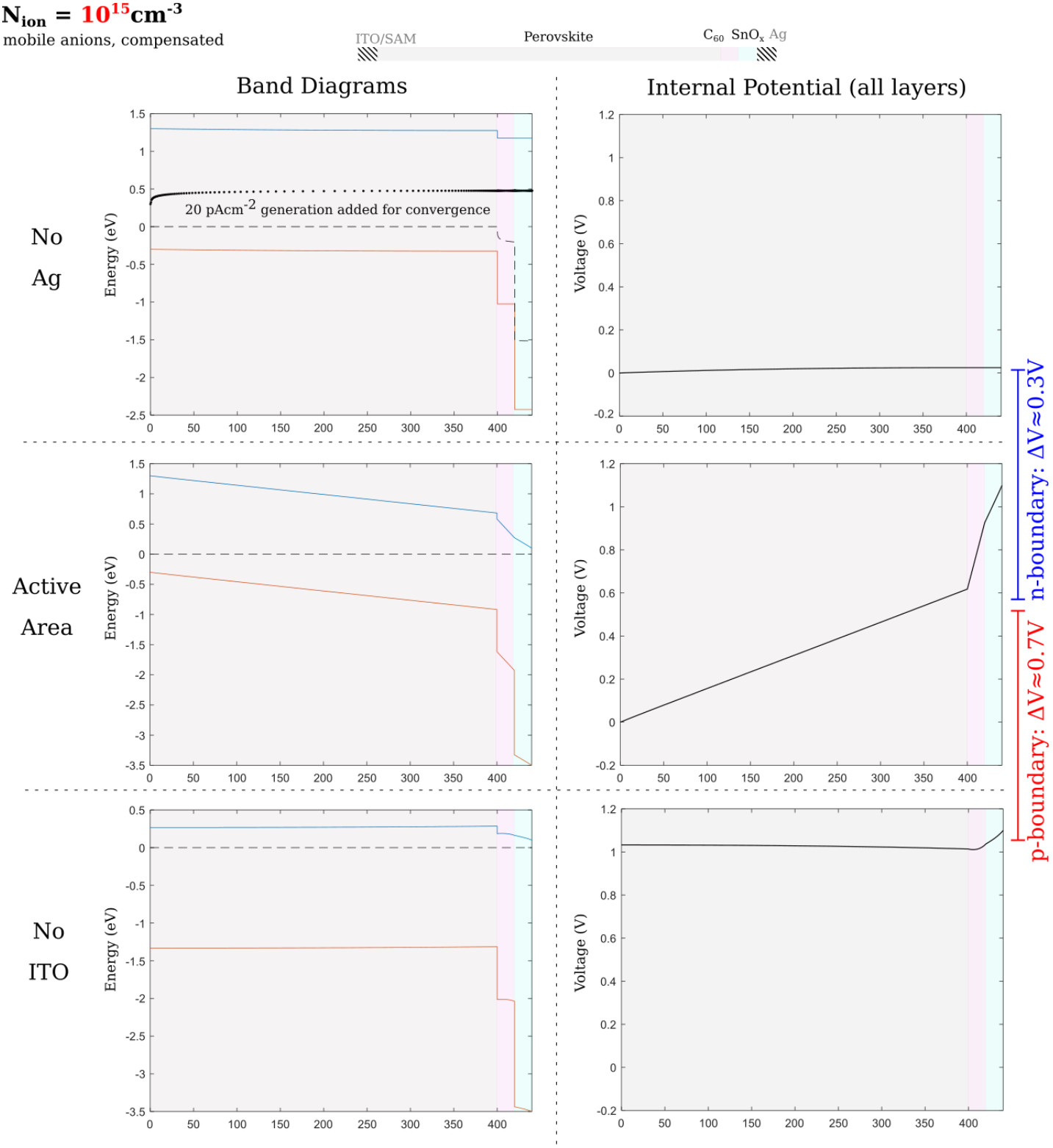

Supplementary Figure M2. 1D drift-diffusion calculations of steady-state band-diagrams (left column) and internal potential (right column) for a low ion density of 10^{15}cm^{-3}. The ITO and Ag electrodes are taken to be at equipotential (0V applied bias). Here the ion density is insufficient to screen electric fields within the perovskite. In consequence, the average internal potential varies significantly at both the n- and p-boundaries. Numerical estimates on the right-hand-side refer to the average internal potential inside the perovskite layer: more precisely, for lateral migration it is the potential on the device side where ions are accumulated that matters most (here, the ETL/right side since our mobile anions accumulate there). To be compared with Supp. Fig. M1.

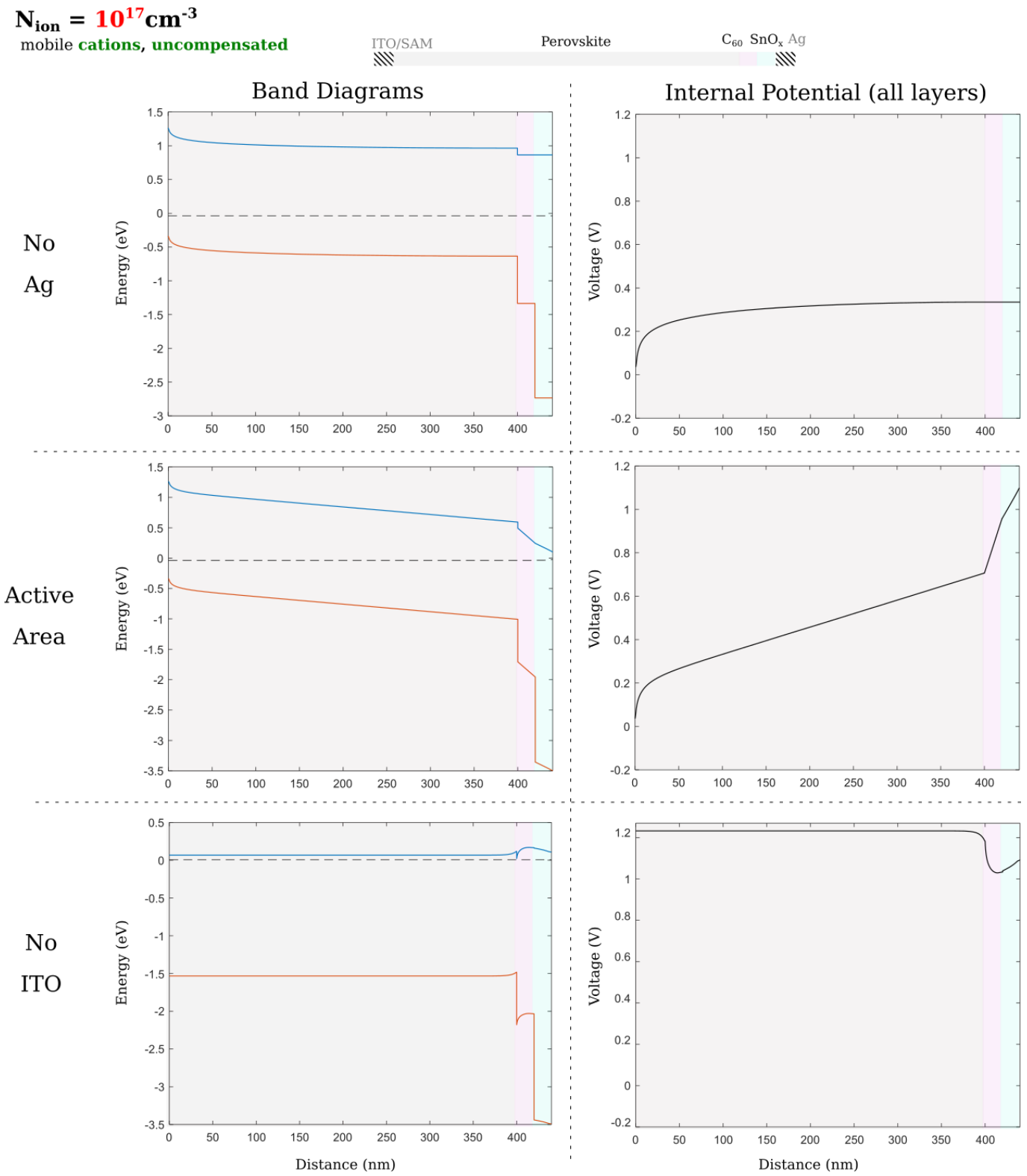

Supplementary Figure M3. n-type perovskite layer. 1D drift-diffusion calculations of steady-state band-diagrams (left column) and internal potential (right column) for a moderately high ion density of 10^{17}cm^{-3}, this time with mobile uncompensated cations (i.e. there is no fixed anion density to compensate the mobile cations, rendering the absorber effectively n-type). The ITO and Ag electrodes are taken to be at equipotential (0V applied bias). Here we see different screening behaviour in each device region according to the presence or absence of either electrode. In the active area and dead-space without Ag, cations are swept to the ITO side where a high interfacial capacitance produces only a minimal potential drop. Only in the ITO-free dead-space do we see a more uniform cation distribution and an n-type band-diagram. Average internal potential varies significantly at both the n- and p-boundaries, however we must recognize that ions in the active area only "see" the potential at the ITO interface due to their accumulation there. Since this potential is nearly invariant at the Ag boundary we would predict low lateral migration at that interface. Conversely, there is a large lateral potential at the ITO boundary for driving ion migration. To be compared with Supp. Fig. M1 and M2.

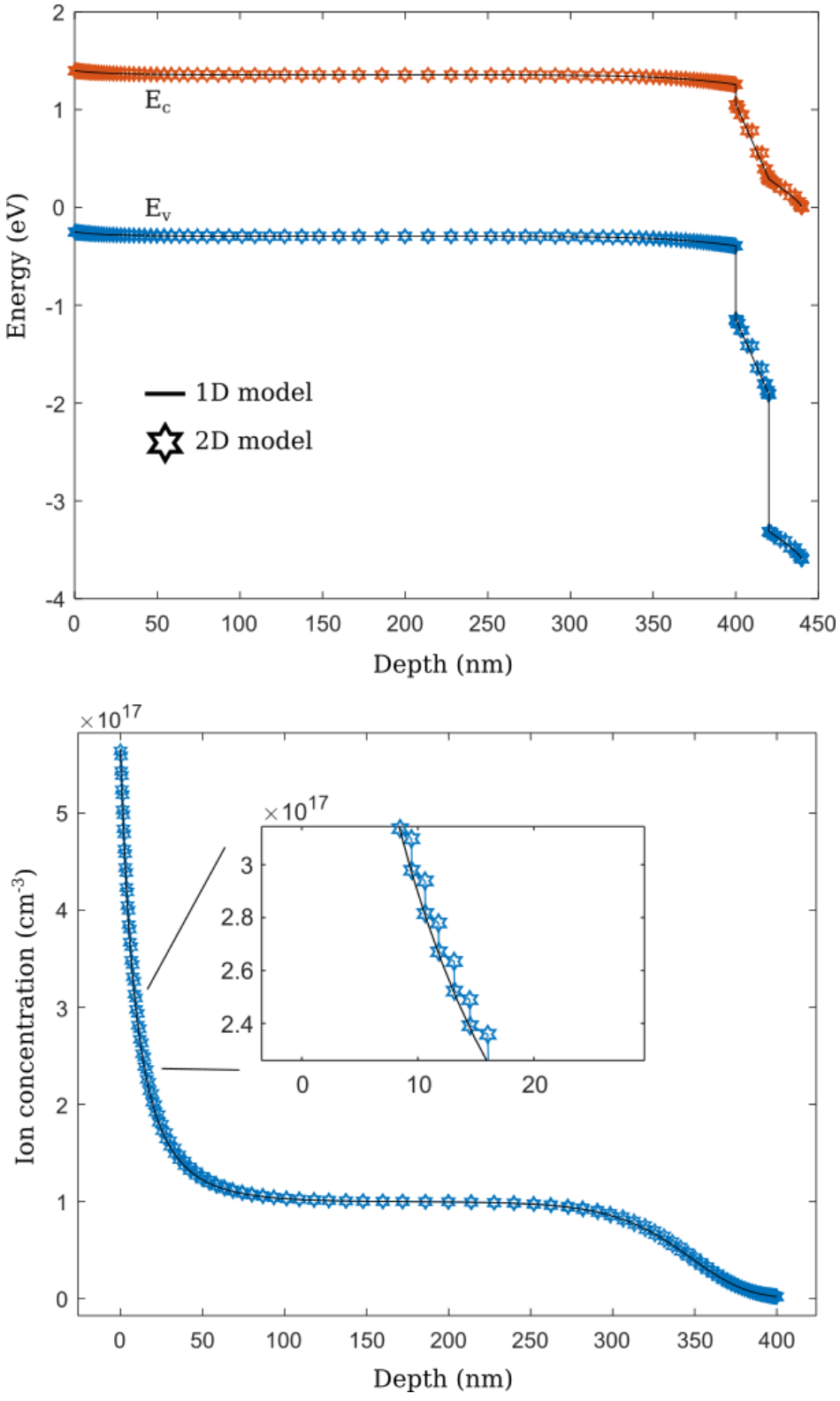

Supplementary Figure M4. Cross-checking our 1D and 2D ionic semiconductor models for consistency. (Top) Band diagram computed within the active area at 0V with an ion density 10^{17}cm^{-3} (mobile cations), shown at 1s after initialization (at this stage lateral effects are unimportant in the region shown, making the 1D/2D comparison possible). Other parameters were set as in the modelling table above. (Bottom) mobile cation density corresponding to the band diagram above. A coarser discretization in our 2D models (for the sake of computational efficiency) results in small errors as visible in the inset. This figure compares favourably with computed ion distributions reported elsewhere (c.f. Figs 3 and 4 of ref [1]).

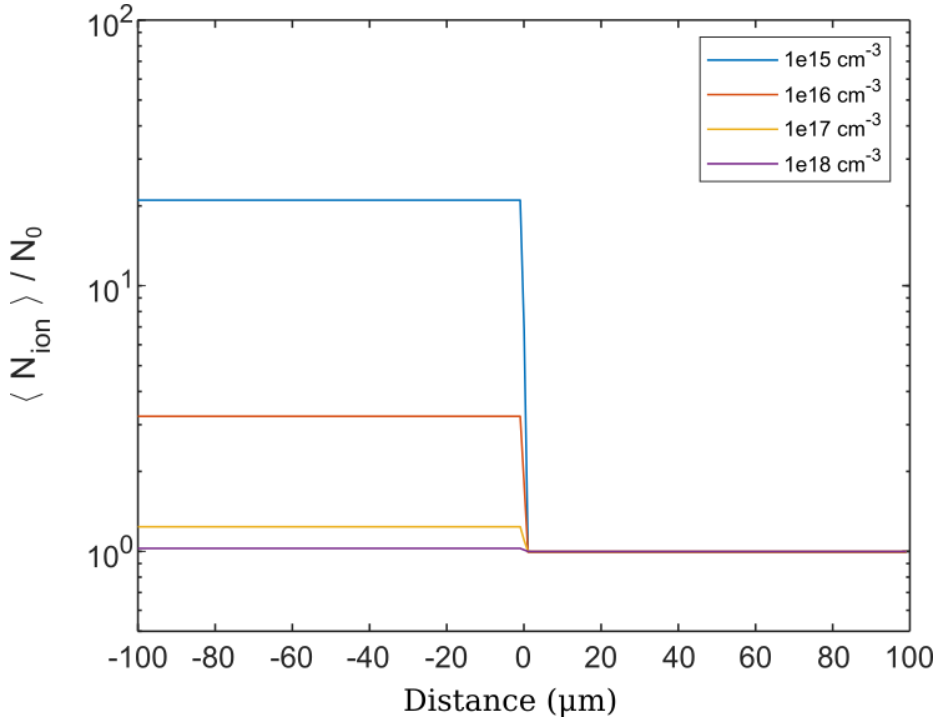

Supplementary Figure M5. Equilibrium anion concentrations (averaged over the film-thickness and normalized to their initial value) for the simulation experiment described in the main text (Fig. 1b), i.e. concerning lateral ion migration under the built-in field at the (n-) Ag boundary of the active area. Devices with higher initial ion concentrations experience less lateral redistribution at this edge as a result of asymmetrical interfacial capacitances, as explained in the main text and as shown in Supp. Fig. M1.

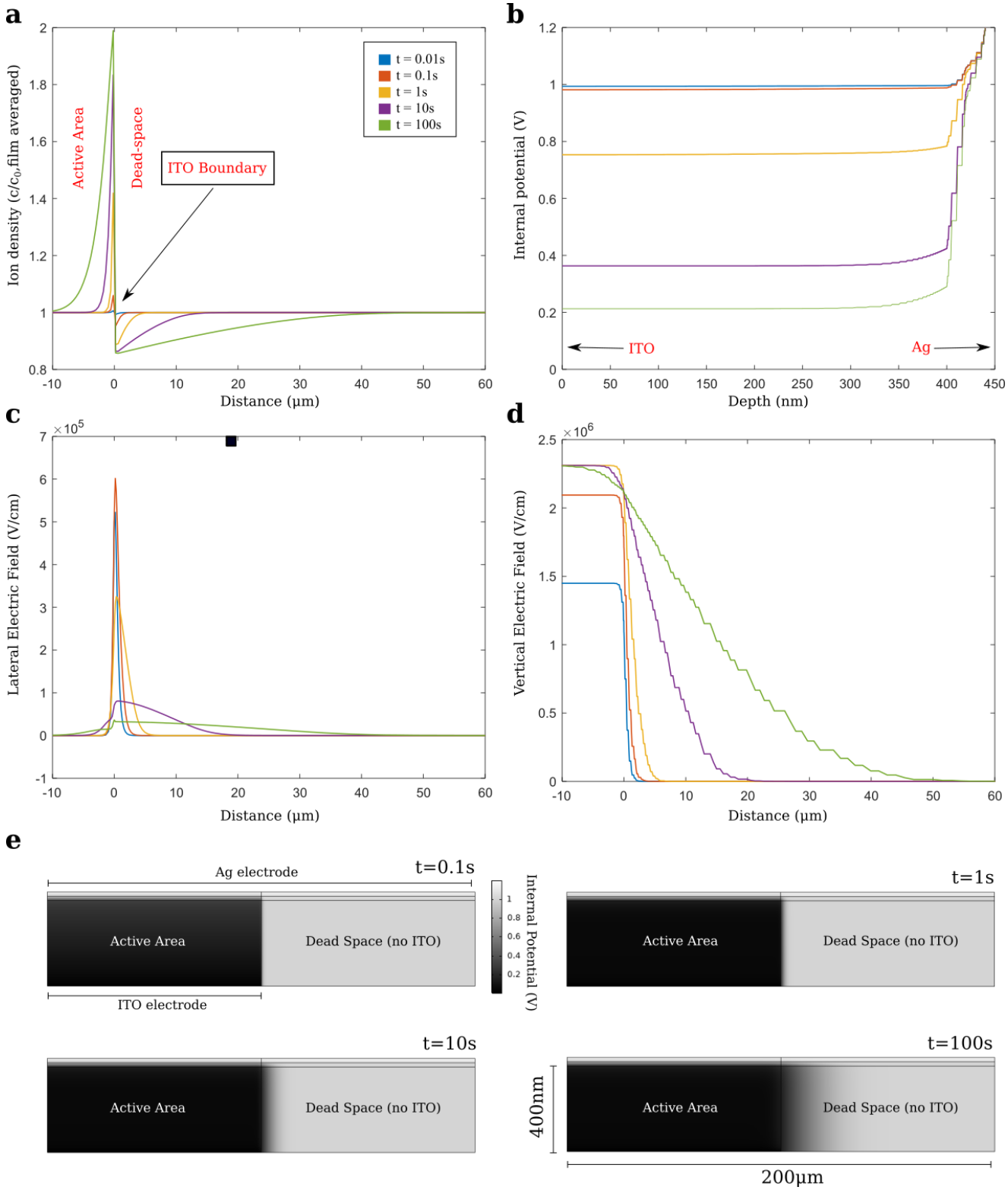

Supplementary Figure M6. Simulation of lateral migration at the p- (ITO-) boundary using our 2D ionic semiconductor models. Here we employ an initial density of 10^{17} cm^{-3} (charge compensated cations) with a diffusion coefficient of 10^{-10} cm^{2}s^{-1}. (a) Plot of the ion density as a function of time across the electrode boundary, normalized to the initial concentration (analogous to Fig. 1b). (b) Internal potential in the vertical (out of plane) direction, measured at a point 2um away from the ITO boundary on the dead-space side, shown as a function of time. It can be seen that space charge left by depleted ions in the dead-space (by the stationary compensating charges) creates polarization at the C_{60}/SnO_x/Ag interface. (c) Lateral electric field strength measured at the top of the perovskite layer (i.e. at the interface with C_{60}) showing that as the ionic space charge spreads into the active area and dead-space, lateral field strength diminishes whereas the vertical field strength measured at the same location (d) does not. (e) Gradient plots of the internal potential across the entire simulation domain (lateral dimension is scaled by a factor of 100), as a function of time.

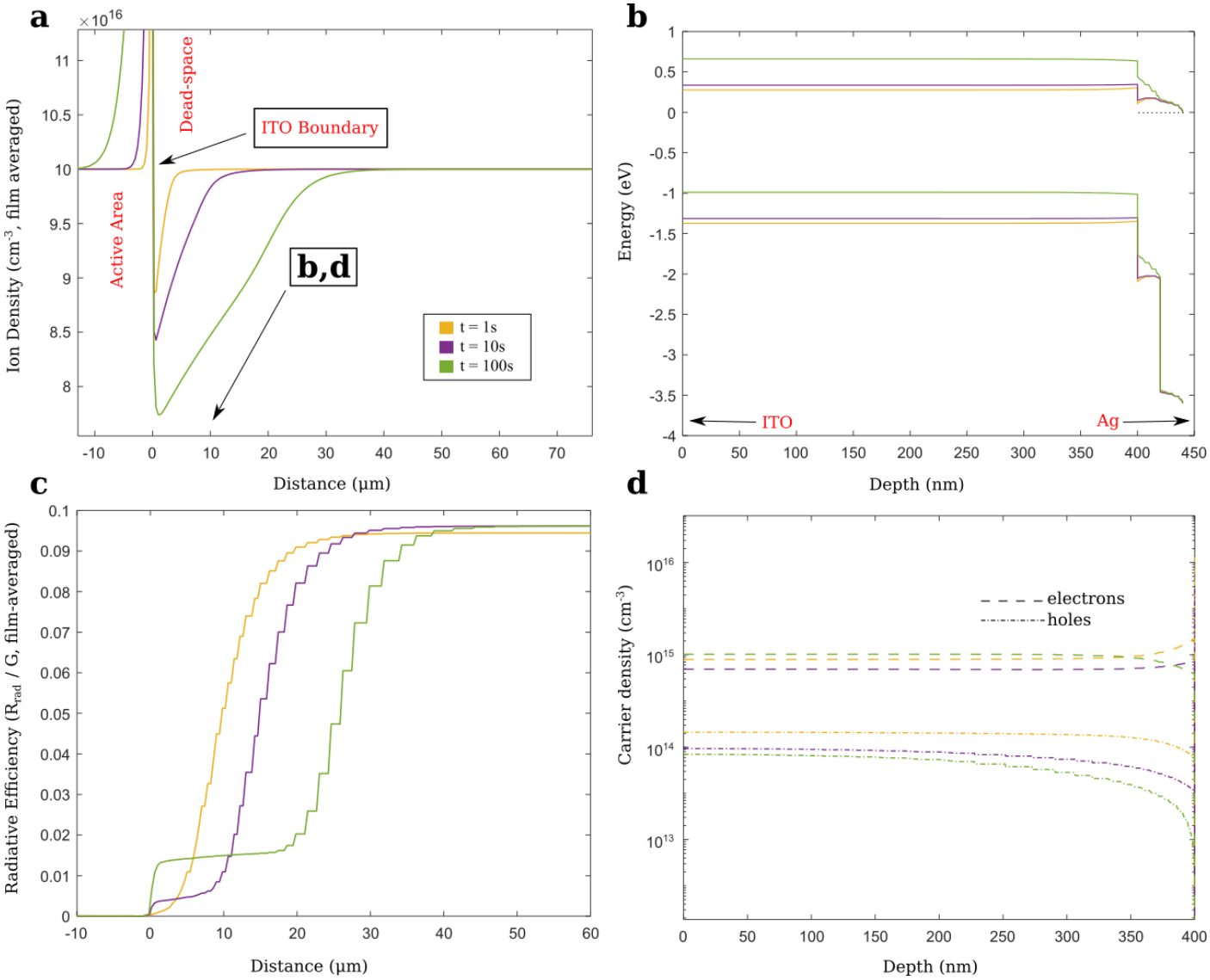

Supplementary Figure M7. Simulation of lateral migration at the p- (ITO-) boundary, using our 2D ionic semiconductor models as in Supp. Fig. M4. Here we employ an initial density of 10^{17} cm^{-3} (charge compensated cations) with a diffusion coefficient of 10^{-10} cm^2s^{-1}. We use an applied voltage of 0V within the active area. (a) ion density averaged over the film thickness as a function of distance from the ITO boundary, and of time after initialization. (b) band diagrams at a point 10μm away from the ITO boundary in the dead-space showing the effect of redistributing ions on the electronic structure (c) radiative efficiency (the bi-molecular rate expressed as a fraction of total generation, with the latter being a uniform rate equivalent to 20mAcm^{-2}) averaged across the film thickness. It can be seen that the radiative efficiency (PL) is affected wherever cations are depleted due to lateral migration into the active area. PL is low within the active area due to the 0V condition applied there. (d) Carrier densities within the absorber in the vertical direction, depicted at the same probe point within the dead-space used for (b), showing the effect of ion migration on carrier distribution and number within the active area.

The recombination model for this simulation comprised a Shockley-Read-Hall term (electron and hole pseudo-lifetimes of 100ns) and a radiative term (B coefficient 10^{-10} cm^3s^{-1}).

[1] H. Shen *et al.*, “Inverted Hysteresis in CH 3 NH 3 PbI 3 Solar Cells: Role of Stoichiometry and Band Alignment,” *J. Phys. Chem. Lett.*, vol. 8, no. 12, pp. 2672–2680, Jun. 2017, doi: 10.1021/acs.jpclett.7b00571.

[2] D. A. Jacobs *et al.*, “The two faces of capacitance: New interpretations for electrical impedance measurements of perovskite solar cells and their relation to hysteresis,” *J. Appl. Phys.*, vol. 124, no. 22, p. 225702, Dec. 2018, doi: 10.1063/1.5063259.

[3] A. Al-Ashouri *et al.*, “Conformal monolayer contacts with lossless interfaces for perovskite single junction and monolithic tandem solar cells,” *Energy Environ. Sci.*, vol. 12, no. 11, pp. 3356–3369, 2019, doi: 10.1039/C9EE02268F.

[4] G. Richardson *et al.*, “Can slow-moving ions explain hysteresis in the current-voltage curves of perovskite solar cells?,” *Energy Environ. Sci.*, vol. 9, no. 4, pp. 1476–1485, 2016, doi: 10.1039/c5ee02740c.